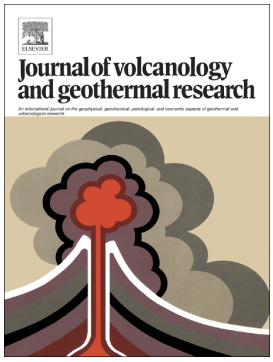

Magnetotelluric imaging of the Ceboruco Volcano, Nayarit, Mexico

Mario Alberto Fuentes-Arreazola, Diana Núñez, Francisco Javier Núñez-Cornú, Armando Calderón-Moctezuma, Diego Ruiz Aguilar, José Manuel Romo-Jones

PII: S0377-0273(21)00168-2

DOI: https://doi.org/10.1016/j.jvolgeores.2021.107339

Reference: VOLGEO 107339

To appear in: *Journal of Volcanology and Geothermal Research*

Received date: 1 June 2020

Revised date: 25 June 2021

Accepted date: 27 June 2021

Please cite this article as: M.A. Fuentes-Arreazola, D. Núñez, F.J. Núñez-Cornú, et al., Magnetotelluric imaging of the Ceboruco Volcano, Nayarit, Mexico, *Journal of Volcanology and Geothermal Research* (2021), https://doi.org/10.1016/j.jvolgeores.2021.107339

Magnetotelluric imaging of the Ceboruco Volcano, Nayarit, Mexico.

Mario Alberto Fuentes-Arreazola[a*], Diana Núñez[a], Francisco Javier Núñez-Cornú[a], Armando Calderón-Moctezuma[b], Diego Ruiz Aguilar[c], José Manuel Romo-Jones[d].

[a] Centro de Sismología y Volcanología de Occidente (SisVOc), Universidad de Guadalajara; Av. Universidad 203, Del. Ixtapa, C.P. 48280, Puerto Vallarta, Jalisco, México.

[b] División de Geociencias Aplicadas, Instituto Potosino de Investigación Científica y Tecnología A.C.; Camino a la Presa San José 2055, Lomas 4ta Sección, C.P. 78216, San Luis Potosí, San Luis Potosí, México.

[c] Cátedras CONACyT-División de Ciencias de la Tierra, Centro de Investigación Científica y de Educación Superior de Ensenada, CICESE; Carretera Ensenada-Tijuana 3918, Zona Playitas, C.P. 22860, Ensenada, Baja California, México.

[d]. Departamento de Geofísica, División de Ciencias de la Tierra, Centro de Investigación Científica y de Educación Superior de Ensenada, CICESE; Carretera Ensenada-Tijuana 3918, Zona Playitas, C.P. 22860, Ensenada, Baja California, México.

*** Corresponding author:** marioafar@gmail.com, mariof@sisvoc.mx

Highlights

- Geoelectrical modeling at the active Ceboruco Volcano from magnetotelluric data.
- Definition of a propitious region to store geothermal fluids.
- Geoelectrical evidence of fractured-permeable basement regions beneath the volcano.

- First geophysical evidence from the clay cap at Ceboruco geothermal reservoir.
- Refinement of geological, geophysical, and hydrogeological conceptual models.

Abstract

Ceboruco Volcano is a Quaternary stratovolcano located in Nayarit near the Trans-Mexican Volcanic Belt western limit. It is one of the most active in the region and the only volcano in Nayarit with historically documented eruptions, the last one between 1870 and 1875. Currently, seismicity and fumarolic activity suggest hydrothermal activity. To study the geoelectrical setting at Ceboruco Volcano and its hydrothermal system, a magnetotelluric exploration campaign was carried out in November 2016, establishing 24 measuring stations at the caldera, and foothills of the volcanic edifice. Three broadband instruments were used in the sampling frequency range of 32768-128 Hz. Recorded time series were processed to determine the MT transfer functions using a robust algorithm and consider the remote-reference station technique. Dimensionality analysis based on the phase tensor determined a shallow 1D geoelectrical structure at periods shorter than 1 s, while a 3D formation was defined at longer periods. To approximate the Ceboruco Volcano substructure, the 3D inversion of magnetotelluric data was carried out. 3D modeling revealed surficial resistivity regions that were related to young volcanic deposits. A relative conductor (10-30 Ωm) was also associated with the shallow regional aquifer. The two most intriguing results of 3D inversion were one uppermost conductive region (~ 1 Ωm) that established characteristics, resistivity, position, and thickness related to a clay alteration minerals zone. The other one (2-5 Ωm) corresponds to a conductive area broadening and fading with depth, centered

slightly to the west of the summit at Ceboruco Volcano. The preferred interpretation of this geoelectrical feature was an envelope of high-temperature fluids, convection of steam, and brines, and they are interacting with the host-rock and surficial groundwater. This geoelectrical feature extends in depth, suggesting a permeable region at the Trans-Mexican Volcanic Belt basement that may be targeted for in-depth geothermal exploration. The geoelectrical setting identified in this study provides information that contributes to reducing uncertainty about the geological, geophysical, and hydrogeological conceptual models at Ceboruco Volcano geothermal system.

Keywords Magnetotelluric Data; 3D inversion modeling; Geothermal fluids reservoir;;; Ceboruco Volcano.

1. Introduction

Ceboruco Volcano (21.125°N, 104.508°W, 2280 m.a.s.l.) is located in Nayarit, Mexico, at the northwestern edge of the Trans-Mexican Volcanic Belt, specifically in the San Pedro-Ceboruco Graben, which constitutes part of the Tepic-Zacoalco Rift (Figure 1). This latter, delineate the boundary between the Jalisco Block and North America Plate, and together with the Chapala Rift and Colima Rift, defines a triple point near Guadalajara city (Nelson, 1980; Stock, 1993; Ferrari et al., 2003).

Ceboruco Volcano is a stratovolcano with emitted calc-alkaline lavas, andesitic-dacitic, whose formation began in the Late Pleistocene; the last eruption of dacitic lava occurred during 1870-1875 (Nelson, 1980; Ferrari et al., 2003; Sieron and Siebe, 2008). In the initial eruptive stages (~ 45 ka), andesitic lavas, with an estimated volume of 60 km^3, formed the volcanic edifice. Approximately 1000 years ago, violent pyroclastic eruptions

occurred, a magma chamber was evacuated, and the top of the mountain collapsed to form the outer caldera of 3.70 km in diameter. Latter, a dacitic volcanic dome was emplaced and subsequently collapsed, creating an inner caldera, 1.50 km in diameter (Nelson, 1980; Ferrari et al., 2003; Frey et al., 2004). In the last 150 years, Ceboruco Volcano has not presented eruptive episodes; however, seismicity and fumarolic activity suggest hydrothermal processes.

In past decades, the Federal Electricity Commission (Spanish acronym: CFE) conducted geological, geochemical, and geophysical studies in the Ceboruco Volcano and surrounding areas to assess its geothermal potential. Nevertheless, the most relevant results were reported in internal-confidential documents. In the last 25 years, research focused on describing geological characteristics, eruptive history (Ferrari et al. 1999, 2003; Gardner and Tait, 2000; Petrone et al., 2001; Browne and Gardner, 2004; Sieron and Siebe, 2008), and geophysical characterization (Venegas, 1995; Sánchez et al., 2009; Rodríguez-Uríbe et al., 2013; Fernández-Córdoba et al., 2017; Sawires and Aboud, 2019; Núñez-Cornu et al., 2020) has been conducted. However, there is still uncertainty in the subterranean spatial configuration of the Ceboruco Volcano and associated hydrothermal activity. This fact was the motivation to carry out a magnetotelluric exploration campaign in November 2016, establishing measurement stations in the calderas, and foothills of the volcanic edifice. This investigation aimed to take advantage of depth exploration and capacity to delimit resistive contrasts of the magnetotelluric method in order to determine the geoelectric subsurface structure of the Ceboruco Volcano. This study's results contribute with relevant information to improve

the geological, geophysical, and hydrogeological conceptual models of the hydrothermal system associated with the Ceboruco Volcano.

2. Tectonic-geological, eruptive history, and hydrogeological setting

2.1. Tectonic-geological setting and eruptive history

Three large-scale regional tectonic domains influence the study area: Sierra Madre Occidental (SMO) in the NNE, Jalisco Block (JB) in the SSW, and the West sector of the Trans-Mexican Volcanic Belt (TMVB), which separates the SMO from the JB (Figure 1).

The SMO is a silicic large igneous province formed by a ~ 1000 m thick plateau of ignimbrites and less rhyolite emplaced in two main periods or flare-up ~32-29 Ma and ~24-20 Ma (McDowell and Clabaugh, 1979, Ferrari et al., 2007). The JB is a fault-bounded crustal block at the western end of the TMVB and corresponds to the Guerrero Terrane west part. Its basement lithologies include metasediments (~240-160 Ma), marine sediments (~140-130 Ma), granitoids (~130 Ma), plutonic rocks (~90-59 Ma), silicic ash tuff (~83-58 Ma), all of which is overlain by SMO ash-flow tuffs and recent volcanic sequences (Valencia et al., 2013).

Ceboruco Volcano (CV) is located in an asymmetric graben known as San Pedro-Ceboruco Graben (SPCG). It is part of a regional-scale depression called Tepic-Zacoalco Rift (TZR) with NW-SE orientation (Figures 1 and 2). This latter is an extensional structure constituted by a set of en-echelon faults that define grabens, semi-grabens that separate the SMO from the JB (Ferrari et al., 2003).

The SPCG is characterized by successive periods of volcanic activity and great tectonic deformation. Ferrari et al. (2003) indicated that the first event of volcanic activity took place 8 Ma ago, produced sequences of basaltic and andesitic lava flows, which covered JB rocks. A succession of Late-Miocene basaltic rocks has been identified in the deep part of CB-1 well drilled by CFE on the southern hillside of CV (Figure 2 and 3), suggesting that the SPCG began its development concurrently with the extension of the proto-Gulf of California (Ferrari et al., 1999). During the Pliocene, the second period of volcanic activity and extensional processes in the SPCG took place. It was characterized by hydrothermally-altered rhyolitic lavas in the West portion and pyroclastic flows in the East sector, dated in 4.6-4.2 Ma, respectively (Gastil et al., 1978; Righter et al., 1995; Frey et al., 2004). Several small cinder cones and few lava domes were emplaced during the Pliocene-Pleistocene in the SSE sector of SPCG, dated in 2.53 Ma and called as Southern Volcanic Chain by Petrone et al. (2001). Many andesitic-rhyolitic lava domes were emplaced in the SPCG central sector during the Pleistocene (Figure 2). The San Pedro domes have the highest peaks and rise inside a 7 to 10 km-wide elliptical caldera (Ferrari et al., 2003). Tepetiltic stratovolcano, composed of andesitic-dacitic lava flows in the NNW sector, and Amado Nervo shield-volcano, constituted by basaltic-andesitic lava flows in the SSW sector, were formed during the Middle-Pleistocene (Ferrari et al., 2003). Cinder cones and domes aligned WNW along 30 km parallel the dominant fault system that limits the northern sector of SPCG were emplaced during the Middle-Late Pleistocene. Most of these monogenetic volcanoes emitted basaltic-andesitic lavas, other dacitic-rhyolitic lavas (Ferrari et al., 2003; Sieron and Siebe, 2008). Also, some volcanoes showed morphological and sedimentary characteristics that suggest a phreatomagmatic activity (Ferrés-López et al., 2019).

Finally, during the Holocene, the extrusion of 60 km^3 of andesitic lava flows (~ 45 ka) built the Ceboruco Volcano (Nelson, 1980; Frey et al., 2004). This first episode of volcanic activity was followed by a period of relative calm, in which Ceboruquito scoria-cone, Cerro Pedregoso, and Cerro Pochetero lava-domes were extruded on the ESE foothill of CV (Figure 2 and 3). About 1000 years ago, a Plinian eruption produced thick-zoned pyroclastic deposits: Jala-pumice and Marquezado-tuff. Also, a magma chamber was evacuated beneath CV, and the top of the volcanic edifice collapsed to form the outer caldera. After, the Dos Equis dacite-dome that partially filled the caldera was extruded. Subsequently, extrusions of dacitic lava-flows undermined the dome causing its collapse forming the inner caldera. The most recent eruption occurred during 1870-1875, initially with small phreatomagmatic-explosions and ash-emissions, after the extrusion of 1.10 km^3 of dacite-lava flowed on the West hillside of Ceboruco Volcano (Nelson, 1980; Gardner and Tait, 2000; Suárez-Plascencia, 1998; Ferrari et al., 2003; Sieron and Siebe, 2008).

At present, CV is in a state of fumarolic activity. Some fumaroles present higher temperatures than 100 °C, suggesting hydrothermal activity (Suárez-Plascencia, 1998; Hiriart-Le Bert et al., 2011; Rodríguez-Uribe et al., 2013). Most fumaroles are located near the 1870-1875 eruption dome (Figure 3) and shown small sulfur deposits (Nelson, 1986). Two other areas of fumaroles have been identified. The one with the highest activity is located in a southern fracture in the outer caldera, while another one with the lowest activity on the western flank of the central dome, both areas of fumaroles, do not show sulfur deposits (Nelson, 1986; Suárez-Plascencia, 1998). Hiriart-Le Bert et al. (2011) suggested that the potential geothermal reservoir would be contained in the

sequence of rocks that constitute the basement of the TMVB, bounded on the surface by an equivalent area occupied by the outer caldera.

2.2. Hydrogeological setting

In the vicinity of CV, three intermittent surface water streams are identified: Ahuacatlán River (E-W drainage direction), Jomulco River, and Jala stream with N-S drainage direction. Several runoff drainages the meteoric water from CV (Figure 1 Supplementary Material). Some of these runoffs define minor structural lineaments that may constitute pluvial water percolation pathways. Four vegetation types dominate the study area (forest, jungle, grassland, and agriculture-lands). This vegetation rise on soils that facilitate meteoric-water infiltration processes (CNA, 2015).

There are no studies about the geological material's hydraulic properties that constitute the Ixtlán-Ahuacatlán regional aquifer near the CV. However, based on the stratigraphic of CB-1 well and geomorphology of CV, three hydrogeological formations can be defined: i) Caldera Formation (CF), meteoric water infiltrates through loose-pyroclastic deposits and fissures caused by extruded domes and runoff erosion. On CF, the water interacts with near-surface steam; thus, fumaroles and occasionally vaporizing soils are observed. ii) Superficial-Regional Formation (SRF) corresponds to the regional aquifer. It is contained in a heterogeneous rocks-sequence constituted by alluvium, rhyolite-andesite-basalt flows, and conglomerate. Groundwater-table (WL) fluctuates around 750 to 1350 m.a.s.l. and shows a regional-flow direction to the southwest (Figure 1 Supplementary Material). Major tectonic and secondary-associated faulting systems represent the percolation routes. iii) Deep Formation (DF), possibly contained in fissures

and fractures on the most deep-seated rocks (andesite-basalt flows, and ignimbrite). Major tectonic-faulting systems correspond to the percolation pathways.

Based on the superficial-groundwater hydrogeochemical analysis (Table 1, CENAPRED, 2015), a slight increment of the concentration of anions-cations, silicon, boron, and water electrical conductivity from NE (Coapan-Village) to SW (Uzeta-Village) direction was identified and concurred with regional-flow direction. The corresponding resistivity values of ~100 Ωm (Coapan) and ~10 Ωm (Uzeta) have been calculated based on water electrical conductivity. However, small ionic concentration changes related to rock-water interaction may be masked by several natural and anthropogenic phenomena. Nevertheless, the chloride and boron concentrations at Ojo de Agua (Cl=9.40±0.17 ppm, B=Undetectable), La Higuera (Cl=19.88±0.17 ppm, B=0.49±0.13 ppm), and Uzeta (Cl=59.58±0.17 ppm, B=1.01±0.29 ppm) were lightly greater than the concentrations (Cl=6 ppm, B<0.1 ppm) reported in local meteoric water by Tello-Hinojosa (1994). The hydrogeochemical setting is beyond the scope of this study, but the rock-water interaction is a plausible cause of the enhanced water conductivity in the Ceboruco Volcano vicinity, and it is a process that required systematic studies.

3. Magnetotelluric data

3.1. Data acquisition

This magnetotelluric (MT) survey includes 24 MT-Stations measured in 2016. The locations of the MT-Stations are shown in Figure 4. The MT-Data were recorded using three ADU07 instruments (Metronix) operated at a frequency range from 32 kHz up to 128 Hz. Disponibility of measurement equipment allowed simultaneous MT-records in at

least two devices installed in different sites. Horizontal electric (E) and magnetic (H) field components were recorded simultaneously in each station's NS and EW directions. The vertical component of the magnetic field was also recorded. The electric field Ex component was measured in the N-S orientation, while the Ey component was recorded in the E-W direction. The distance between electrodes was approximately 100 m. The magnetic field Hx component was recorded using an N-S oriented induction coil; while the Hy component with an E-W oriented coil. A third induction coil was used to record the vertical component (Hz) of the magnetic field. Four sampling rates were selected to record the variations of electromagnetic fields at MT-Stations: the HF band (sampling frequency (SF) 32768 Hz, recording time (RT) 30 min), the LF1 band (SF 2048 Hz, RT 4 h); the LF2 band (SF 512 Hz, RT 12 h); and the LF3 band (SF 128 Hz, RT 60 h). As a result of logistic difficulties in the acquisition, it was impossible to record the four sampling rates in all MT-Stations, or simultaneously in at least two instruments (Table 1). Based on those mentioned earlier and the low quality of the recorded EM fields, 8 MT-Stations were not considered for processing and analysis.

3.2. MT data processing and analysis

The recorded time series at 16 MT-Stations were processed to compute the magnetotelluric response functions using the Bounded Influence Remote Reference Processing (BIRRP) robust algorithm (Chave and Thomson, 2003, 2004). Although a proper remote reference MT-Site was not settled down during the field survey, the remote reference processing technique was applied using magnetic data from MT-Sites with a simultaneous recording (Gamble et al., 1979).

The robust processing scheme results in a period band ranging from 0.001 to 100 seconds are shown in Figure 5 at four selected stations to illustrate the data quality. Transfer functions estimations at periods greater than 100 s showed unsatisfactory quality. Data from CB01 and CBF3 are typical of those sites located at the lower elevation (1000-1400 m.a.s.l.) zone within the study area. Data from CB23 and CB24 represent those located at a higher elevation (1900-2200 m.a.s.l.). Please note that at CB24, the electromagnetic fields were recorded only at 32768 Hz sampling frequency. The XY-YX modes of apparent resistivity curves in each MT-Site were similar in shape. Generally, all MT-sites showed resistivity values ranging from 1000 to 1 Ωm. A typical pattern in the resistivity and phase curves was observed at lower elevation sites; they remain parallel for short-intermediate periods and exhibit a split between XY-YX curves for periods higher than 1 s. This latter possibly indicates a shallow 3D geoelectrical structure covered by a 1D superficial one. Transfer functions computed for the four impedance tensor components at 16 MT-Stations are shown in Figure 2 of Supplementary Material. A great source of anthropogenic noise corresponds to the telecommunications facilities located in the northern sector of CV crater, at one kilometer apart from CB12 and seven kilometers far away from CB01 (Figure 4).

To provide an overview of the dimensionality of the complex geoelectrical structures associated with the Ceboruco, the phase tensor (PT) of Caldwell et al. (2004) has been used. PT is insusceptible to galvanic distortions and can be represented graphically as an ellipse (PT-ellipse) with the principal axes (Φmax and Φmin) showing the major-minor axes of the tensor. These latter axes are related to defining the ellipticity parameter (λ). If the phase-tensor ellipse is non-symmetric, a fourth parameter

represented by the skew-angle (β) is needed to characterize the tensor. The dimensionality of the MT-Data at any period may then be assessed according to the following criteria (Bibby et al., 2005): i) $\lambda \approx 0$, $\beta \approx 0$: 1D; ii) $\lambda \neq 0$, $\beta \approx 0$, azimuth (α-β) constant: 2D, and iii) $\lambda \neq 0$, $\beta \approx 0$ or $\beta \neq 0$, but azimuth (α-β) no constant: 3D.

According to the β-value at all MT-Stations, PT-ellipses color-coded is displayed at four different periods (0.01, 1, 10, and 100 s) in Figure 6. At short periods (0.01 s), PT-ellipses at all MT-Sites were approximately circular, indicating a 1D geoelectrical structure. The exceptions to this are the CB12 and CB22 MT-Sites. As the period increases, commonly exist an increment in the complexity of the PT-ellipses behavior. At the rest of the periods, all the PT-ellipses were mainly represented by ellipses with $\beta \neq 0$, indicating a 3D structure. The dimensionality analysis shows that PT indicates a 1D structure for periods < 1 s and a 3D structure for periods > 1 s. Consequently, to determine the geoelectrical structure of the Ceboruco Volcano, a three-dimensional inversion modeling approach was conducted.

3.3. MT data 3D inversion

The 3D modeling of the MT-data acquired in CV was performed using the ModEM algorithm (Kelbert et al., 2014). The full impedance tensor components were included. Topography information was also taken into account within the inversion scheme, so no static shift correction was needed (Arnason, 2008). To efficiently use the 3D inversion program, only four periods for decade were selected, thus reducing the size of the data (N) and memory size and CPU time. The model (M) size was given by the discretization of 60 x 66 x 73 nodes in the x, y, and z directions, respectively. The horizontal

discretization within the data coverage was set to 250 x 250 m size cell. Ten padding cells with an increasing factor of 1.3 were also included. To consider the topography variations, 29 layers of 50 m thickness, followed by 44 layers logarithmically increasing thicknesses (factor 1.2), were defined. As a result of inversion trials, a 30 Ωm homogeneous half-space was determined as the starting model for the inversion. Data errors were set to 5% of abs (Zij) for the off-diagonals and 10% for the main diagonal components. The initial value of the regularization parameter was 1, and an isotropic smoothing parameter of 0.3 was used. After 133 iterations, a global root mean square error (RMS) of 1.92 was reached.

In Figure 7, profiles extracted from the 3D inversion model are shown. Simultaneously, the fits of the inversion to observed data from 16 MT-Stations are presented in Figure 3, Supplementary Material. The 3D inversion model suggests the presence of several geoelectrical features. A resistor denoted as R1 (> 500 Ωm) at shallow depths was identified in the western crater sector and showed a thickness of a few hundreds of meters (profile A1-A2, Figure 7). Another thin resistor R2 (200-400 Ωm) at lower elevations (~ 1000 m.a.s.l.) was recognized, data of seven MT-Stations constrain its thickness (100-200 m) and lateral continuity at the eastern to southwestern CV region (profiles B1-B2, C1-C2, D1-D2, Figure 7). A third shallow depth relative resistor R3 (100 – 200 Ωm) was distinguished in the uppermost layer at CV. The conductor indicated as C1 (~ 1 Ωm) was identified at the top-central portion of the extracted profiles and appeared to be laterally constrained at the caldera sector. Another conductor, C2 (2-5 Ωm), was recognized at the central sector and extended towards the maximum depth model. Finally, a relative conductor C3 (10-30 Ωm) was distinguished at low depths in

the model calculated. Due to the relatively large distance between MT-Stations, the information of the penetrated EM waves recorded at each site cannot be interconnected at such depths. Consequently, some geoelectrical features are isolated.

3.4. Validity of the inversion model

The conductive anomaly C2 beneath the CV is one of the most intriguing results revealed by the 3D inversion modeling. The data sensitivity to the size, shape, and resistivity value of this structure was tested by replacing the resistivity to 100 Ωm in cells from -2000 to 10000 m.a.s.l. (model SAM1). The misfit of this model response resulted in an RMS value of 1.98 compared to 1.92 obtained from the final inversion model (Figure 4, Supplementary Material), meaning that the data set seems slightly sensitive to the presence of C2. A second test consisted of reducing the size and resistivity value of C2 to simulate an elongate-vertical shape with 3 km in diameter and 1 Ωm (model SAM3). The RMS obtained from this new test model was 2.25 (Figure 4, Supplementary Material), suggesting that the best solution for the C2 is a conductive feature broadening and fading with depth, as obtained by our final inverse model (Figure 7). We did a third sensitivity experiment to test the connection between C1 and C2 (model SAM2). A constant value of 30 Ωm replaced the resistivity of the cells connecting both conductive anomalies from 0 to -4000 m.a.s.l. The resulting RMS was 1.93 (Figure 4, Supplementary Material), evidencing that data sensitivity is insufficient to determine the separation between C1 and C2. To summarize, we believe that the final inverse model shown in Figure 7 adequately explains the observed data and is a geologically plausible image of the resistivity distribution beneath the CV. However, the depth at which C2 extends is not well constrained as a result of several causes: i) investigation depth

limited by MT data at 100 s as maximum period, ii) not optimal coverage of MT-Stations around the volcano, and iii) the inherent 3D nature of the structures beneath at CV.

4. Interpretation and discussion

Ceboruco Volcano lies in a complicated and inherent 3D setting that corresponds to TZR active faulting tectonic system that defines the boundary between the SMO and JB. On CV, the MT soundings show a typical geoelectrical pattern related to high enthalpy geothermal systems, consisting of a top resistivity layer that overlies a conductor, followed by a relative resistive layer covering a conductive half-space (e.g., Cumming and Mackie, 2007; Spichak and Manzella, 2009). Conductive and resistive features determined at the 3D inversion model are correlated to the geological, geophysical, hydrothermal, and hydrogeological CV settings.

In this regard, the top resistive bodies (R1>500 Ωm, R2=200-400 Ωm, and R3=100-200 Ωm) show resistivity values typical for young-unaltered volcanic rocks. Particularly, R1 (Figure 7) agrees with the location of the 1870 dome and associated lava flow (Figure 3). Concerning resistive body R2, it is related to Ceboruco pre-caldera, Copales lava flows, and the surficial Quaternary volcanic breccia (Figures 2-3) associated with monogenetic volcanoes (e.g., Ceboruquito, Pedregoso, and Pochetero) at the southeastern sector. The relative resistor body R3 is linked with the andesitic lava flows that constructed the earlier CV edifice that was subsequently fractured and altered due to recent volcanic activity.

As observed in this investigation and previous geoelectrical studies (Venegas, 1995), resistive surficial volcanic rocks overlie conductive regions. Several geological materials,

active faulting systems, and hydrological processes may explain low resistivity zones in volcanic settings. Geothermal fluids (high concentration of dissolved salts) and clay alteration minerals (CAM) present a high-conductivity signature and are commonly associated with volcanic geothermal reservoirs.

Alteration minerals constitute the confining cap for most of the hydrothermal systems. At lower temperatures (70-150 °C), the clay cap is mainly characterized by the smectite clay group. At higher temperatures, ilite-group (in acid rocks) and chlorite (in basaltic rocks) become interlayered with smectite. The alteration shows a higher resistivity signature in the form of chlorite and epidote minerals than its lower temperature counterparts. The low-temperature alteration species are significantly more conductive than the more elevated temperature species (Bjornsson et al., 1986). Ussher et al. (2000) reported a comprehensive review of the causes of enhanced electrical resistivity in geothermal systems. A relevant conclusion was that an increase in resistivity beneath a highly conductive surficial layer (clay cap), reflecting an increase in temperature with depth, is a characteristic signature of high-temperature volcanic geothermal systems. Clay caps and adjacent hydrothermal systems feature typical resistivities of <10 Ωm (smectite), ≤10 Ωm (ilite-smectite), and ≤100 Ωm (ilite-chloride) (Wright et al., 1985; Pellerin et al., 1996).

Material recovered from drilling the CB-1 exploration-well showed some insights into low-temperature clay alteration minerals (Figure 3). Calcite was identified on micro-faults at cores recovered, and its formation temperature (137 °C) was determined by fluid inclusion analysis. Besides, plagioclases, chlorite, zeolites, and quartz replacements were observed (Venegas, 1995). CB-1 well was drilled at the southwestern flank at the

Copales lava flows, and the temperature log (Tmax=115 °C) shown a normal geothermic gradient (Hiriart-Le Bert et al., 2011). This latter feature agrees with the isothermal contours observed in the geological conceptual model (Figure 8) proposed by Venegas (1995). In this regard, no relevant conductive bodies were defined from magnetotelluric data in the vicinity of the CB-1 borehole.

Position and resistivity ranging values (~ 1 Ωm) of the C1 conductive body suggest surficial geothermal fluids and clay cap commonly observed in volcanic hydrothermal systems. The potential CV hydrothermal system's major features are the fumarole fields (~100 °C) in the caldera sector (Figure 3). Chemical evidence suggests that CO_2 concentrations are mainly related to local meteoric water. In contrast, H_2S concentrations are the signature of deeper fluids sources. CO_2 presence on fumaroles may also be related to degassing of fluids when calcite deposition occurs and contributions from sedimentary carbonate basement (Viggiano-Guerra, 1993).

Regarding the clay cap, a low-temperature alteration mineral has been identified on the material recovered from drilling the CB-1 exploration well, 4-5 km away from the CV caldera sector. However, clay alteration mineral has not been reported in the vicinity of the CV caldera. Therefore, the conductor body C1 resulting from the 3D inversion model contributes to determining the hydrothermal clay cap (Figures 7-8). The resistivity values of C1 are comparable with those related to the smectite clay group (<10 Ωm), which is typically formed at temperatures ranging between 100-200 °C. The top of the conductor body C1 is indeed defined at profiles extracted from the 3D inversion model. However, its bottom limit is not delineated, probably as a consequence of ascending hydrothermal fluids and local groundwater interaction.

Venegas (1995) determined a regional shallow conductive layer (<30 Ωm) as a result of a geoelectrical campaign that consisted of 178 vertical electrical surveys and 90 magnetotelluric sites. Conductive anomaly extends from Jala to San Pedro Lagunillas. Its top was identified at least 100 m below terrain level and showed sectors whit thickness greater than 400 m, one of them beneath the CV. The conductive body C3 (10-30 Ωm) identified in the 3D inversion model is comparable on resistivity and depth with the regional conductivity anomaly reported by Venegas (1995). The resistivity of C3 is congruent with those typical values associated with groundwater (10-100 Ωm). The water level at the regional aquifer fluctuates around 750-1350 m.a.s.l. and shows a preferred-flow direction to the southwest (Figure 1, Supplementary Material). At the central sector in the volcano base, it is impossible to distinguish electrically between the presumable clay alteration minerals and local groundwater, which have low resistivity (Figure 7). Lateral extension and lower resistivity values of C3 may be explained as a result of rising hydrothermal fluids and local groundwater interaction. The outflow of these subsurface waters will follow the natural groundwater drainage and trace the C3 body's upper surface. Besides, warm water (20-30 °C) can be found in some natural springs and agricultural-wells on the volcano's lower flanks (CENAPRED, 2015). The chloride and boron concentrations at Uzeta village are mainly greater concerning local meteoric water concentrations (CENAPRED, 2015). Therefore, the rock-water interaction is a plausible cause of the enhanced water anions-cations concentration in the CV vicinity. However, small ionic concentration changes related to rock-water interaction may be masked by several natural and anthropogenic phenomena. Nevertheless, it is a process that should not be discarded and required detailed studies.

The 3D inversion models showed that the best solution for the C2 is a conductive feature broadening and fading with depth beneath the summit Ceboruco Volcano (Figure 7). Similar resistivity signatures have been observed associated with stratovolcanoes. At Mount St Helens and Mount Adams volcanoes, a conduit-like zone of high electrical conductivity (<10 Ωm) at 15 km depth was interpreted to be a region of connected melt that acts as the reservoir for the silicic magma being extruded (Hill et al., 2009). A similar shallow (< 3 km b.s.l.) near-vertical conductive structure (<10 Ωm) at Telega-Bodas geothermal field was interpreted as a vapor-dominated chimney that provides a pathway to the surface for magmatic gases (Moore et al., 2008). A narrow conductive dike-like feature was interpreted as a conduit by which water and gases of volcanic origin have moved from depth to surface at Mount Ruapehu volcano (Ingham et al., 2009). A subvertical-low resistivity (< 1 Ωm) column-shaped body beneath Naka-dake crater, Aso volcano, that extends from -0.6 to 10 km b.s.l. was interpreted as a magmatic-hydrothermal system composed of brine and magma transported from the main deep-seated magma reservoir (Matsushima et al., 2020).

Magmatic geothermal reservoirs include convective hydrothermal-enveloping (water and steam dominated), hot dry-rock, or partial melt systems (Muñoz, 2014). Therefore, C2 could be related to the volcanic conduit by which hot volcanic fluids and, potentially, magma are transported to the surface from a deeper heat source that propitious a shallow partial melting. In the model presented in Fernandez-Cordoba et al. (2017), the negative Bouguer anomaly computed was related to a shallow-magma chamber located about 1 km b.s.l. and has a volume of 163 km3. In addition, a positive magnetic anomaly

derived from aeromagnetic data inversion was related to a subsurface magma chamber above the TMVB basement (Sawires and Aboud, 2019).

In this sense, petrological analysis (Nelson, 1980; Luhr, 1992) suggests that andesitic-dacitic lavas erupted from CV have values of SiO2 (51 – 74 wt.%), temperature (810 – 1045 °C), and water content (0.5 – 3.0 wt.%). These features can be associated with a melt resistivity between 0.34 and 30.85 Ωm for an andesitic model (Laumonier et al., 2017), and 0.81 and 13.31 Ωm for a dacitic model (Laumonier et al., 2015) at pressures of 0.5 GPa (14-16 km in-depth), and 0.15 GPa (4-5 km in-depth), respectively (using Sigmelts Poomier and Le Trong, 2011). The defined resistivity values of C2 (2 – 5 Ωm) are comparable to those predicted values for a dacitic model. Thus, C2 would be related to a possible magmatic source for the recent CV dacitic lavas.

A modified Archie's law (Glover et al., 2000) was used to compare the resistivity values computed according to the lavas composition and comparing them with the resistivities obtained through the inversion modeling (Figure 9a). The low resistivity of C2 can be explained in terms of a minimal fraction melting of 40 – 63 % (felsic model, 3.0 wt.% H2O), and 20 – 46 % (intermediate model, 0.5 wt.% H2O). In general, these values appear physically improbable at these depths. Unfortunately, information regarding the melting fraction of the CV erupted dacitic lavas is inexistent. Particularly, fraction melting computed values for an intermediate model are comparable to those values required (10 – 30 %) to produce the andesites that constructed the Ceboruco volcanic edifice, ~ 45 ka (Nelson, 1980). While a shallow magma chamber fed the Ceboruco recent eruptions, this amount of melted rock at these depths is implausible today. This latter based on relatively low-temperature logging at exploration CB01-well (Tmax = 115 °C) and low-

temperatures at fumaroles areas (~ 100 °C). The C2 bulk resistivity is difficult to explain without including large amounts of dissolved water in the melt to increase the conductivity (Laumonier et al., 2017). Added to this, the magmas from Ceboruco have significantly lower water contents compared to the more hydrous magmas from Colima volcano, another active volcano at the western portion of the TMVB (Luhr, 1992). Values of partial melt that are high and inconceivable could instead be explained by the presence of saline fluids of magmatic and/or meteoric origin, as Pritchard et al. (2018) inferred.

In this regard, another possible source of low resistivity could be attributed to the presence of high-temperature fluids, convection of steam and brines, and their interaction with the host rock, the basement of the TMVB (Figures 7-8). Chemical evidence at CV fumaroles suggests that CO2 concentrations are mainly related to local meteoric water. However, CO2 presence may also be related to degassing of fluids when calcite deposition occurs and contributions from sedimentary carbonate basement. In addition, H2S concentrations are the signature of deeper fluids sources (Viggiano-Guerra, 1993). On the other hand, hydrogeochemical surficial-groundwater analysis indicates lightly greater chloride and boron concentrations than the meteoric water observed values (Tello-Hinojosa, 1994), suggesting a plausible rock-deeper fluids interaction. Therefore, the geoelectrical feature C2 could be evidence of the storage, ascending movement, and exchange of geothermal fluids beneath the CV.

The bulk resistivity of a geothermal fluid (NaCl ~ 1000-10000 ppm) has low resistivity values (1.00, 0.10, and 0.01 Ωm) at temperatures ranging from 200 to 300 °C (Unsworth and Rondenay, 2013). These resistivity values were compared with those values

obtained through the inversion modeling using a prediction model based on Archie's law (Figure 9b). The low resistivity of C2 (2 – 5 Ωm) can be explained considering a brine (0.10 Ωm) contained in an interconnected rock porous-phase ranging between 5 and 13.5% with a saturation ratio of 75 to 100 %. Another possible explanation is a brine (0.01 Ωm) in a rock porous-phase ranging from 1 to 3% with a saturation of 75 to 100 %. The porosity values required to explain C2 as a structure saturated by a brine of 0.10 Ωm are comparable with those values used (min = 5%, max = 18%) to estimate the geothermal potential associated with the CV hydrothermal system (Hiriart-Le Bert et al., 2011). The relative massive size of C2 can be associated with brine and vapor enveloping beneath the CV. If brine exsolution is assumed to be caused by deep-seated solidifying magma-chamber, then such brine would need to ascend and accumulate in shallower depths (Shinohara, 1994; Matsushima et al., 2020). Based on the above, the possibility of the coexistence of a small-scale shallow ancient magma chamber enveloped by geothermal fluids is not ruled out. Despite that, a small-scale magma chamber or magmatic conduits directly below a volcanic edifice are challenging to resolve using MT data (e.g., Díaz et al., 2015, Mancini et al., 2019).

As a consequence of the not optimal coverage of MT-Stations around the CV, the C2 lateral limits are not well defined. However, based on structural lineaments, it is possible to constrain them. Recent seismic activity at CV has shown epicentral distribution around the volcanic edifice along three structural lineaments (Núñez-Cornú et al., 2020): SLA is located at the northwestern sector at CV; SLB at the southwestern portion of CV; and SLC at the southern sector of CV. In addition, the buried inferred fault (I.F. SE-NW) associated with the WNW trending alignment of cinder cones and lava domes (Ferrari et

al., 2003) cross the volcanic edifice from east to northwest direction. These structural lineaments show a remarkable correlation with the C2 lateral limits (Figure 7 and Figure 1, Supplementary Material), defining pathways for geothermal fluids ascending to the regional aquifer and facilitates the CV's recharge hydrothermal system.

In overview, the magnetotelluric data of this study defines a conductive region that corresponds to a propitious storage-space for a zonal geothermal reservoir constrained at the caldera sector based on structural lineaments and which extends at least 5 km b.s.l. Since fracture permeability is required to transport heat through the basement convectively, the MT results suggest that low-resistivity zones in the basement of the TMVB indicate permeable regions that may be targeted for in-depth geothermal exploration (Figure 8). The zonal geothermal reservoir's size and shape reported in this work are quite similar to those of the geothermal system described by Hiriart-Le Bert et al. (2011). However, its bottom limit is not delineated; and the presence of a small-scale ancient magmatic chamber is not discarded. Therefore, an equally-spaced regular grid of broadband MT-Sites is crucial to improve the geothermal target beneath the Ceboruco Volcano.

5. Conclusions

Ceboruco Volcano sits in a complex tectonic, geologic, and hydrogeological setting, and its underground configuration is poorly known. A dimensionality analysis of MT-Data was carried out based on the phase tensor, which suggested a shallow 1D geoelectrical-structure for periods shorter than 1 s at most of the MT-Sites. In comparison, a 3D structure was defined for longer periods. Therefore, a 3D inversion of MT data was

carried out to determine the deeper Ceboruco volcano-structure. Profiles extracted from the 3D model defined surficial resistivity bodies that were related to young volcanic deposits. A shallow conductor (10-30 Ωm) was linked with the regional aquifer. Two major conductive features, C1, and C2 were also revealed. The shallowest one, C1 (~ 1 Ωm), was interpreted as the hydrothermal reservoir clay cap and corresponded to the first insights of this feature at the Ceboruco volcano hydrothermal system associated. The C2 conductive feature (2-5 Ωm) was analyzed by predicting their resistivity using a melting-rock model and a rock saturated-porous model, both based on Archie's law. Considering the composition of lavas, temperature, pressure, and water content, the computed values of C2 were explained by a high melting fraction between 20 and 63%. However, these values are physically improbable at these depths and under the normal thermal gradient observed at Ceboruco today.

On the other hand, the combination of a rock-host with a porosity between 5 to 13%, a brine of 0.10 Ωm, and a saturation ranging from 75 to 100% were required to explain C2 low resistivities. The set of MT data analyzed in this study did not resolve a magmatic chamber. The modeled resistivity values and porosity-saturation conditions were more consistent with those typically observed at a high enthalpy hydrothermal-reservoir water dominated. However, the possibility of the coexistence of a small-scale, shallow ancient magma chamber enveloped by geothermal fluids is not ruled out.

Therefore, the preferred interpretation of the conductive feature broadening and fading with depth denoted as C2 was an envelope of high-temperature fluids, convection of steam and brines, and interacting with the host-rock and surficial groundwater. This geoelectrical feature extends in depth, suggesting a permeable region at the Trans-

Mexican Volcanic Belt basement that may be targeted for in-depth geothermal exploration. A complementary equally-spaced regular grid of broadband MT-Sites is crucial to improve the Ceboruco Volcano geothermal target.

Data and Resources

All magnetotelluric data are in a database at Research Group 276 Centro de Sismología y Volcanología de Occidente (CA-UDG-276-SisVOc). The data may be available for collaborative research projects between CA-UDG-276-SisVOc and other interested institutions by specific agreements. For information, contact pacornu77@gmail.com.

Acknowledgments

This research was funded by the project: Centro Mexicano de Innovación en Energía-Geotérmica (CeMIE-Geo). P24. Exploración sísmica pasiva y magnetotelúrica en los campos geotérmicos de Volcán Ceboruco y La Caldera de la Primavera. SENER-CONACYT 201301-207032. Mario Alberto Fuentes Arreazola was funded by a Postdoctoral scholarship from Programa para el Desarrollo Profesional Docente, Secretaria de Educación Pública. Apoyos posdoctorales en Cuerpos Académicos Consolidados (Oficio: 511-6/18-11386), and the services contract (CGSAIT/CUCOSTA-2860/2020). The authors would like to thank the Supercomputing Lab of SLECT from CICESE for allowing to use the cluster LAMB to perform the 3D modeling of the MT data. Thanks are extended to Naser Meqbel for providing us his 3D Grid-Tools software.

References

Arnason, K. **2008**. The magneto-telluric static shift problem. Iceland GeoSurvey Report ISOR/08088. Reykjavik, Iceland, 17 pp.

Bibby, H.M., Caldwell, T.G., Brown, C. **2005**. Determinable and non-determinable parameters of galvanic distortion in magnetotellurics. *Geophysical Journal International*, **163**(3), 915/930. doi:https://doi.org/10.1111/j.1365-246X.2005.02779.x

Bjornsson, A., Hersin, G.P., Bjornsson, G. **1986**. The Hengill high-temperature area, SW-Iceland: Regional geophysical survey. *Transactions of the Geothermal Resources Council,.*, **1986**(10): 205-210.

Browne, B.L., Gardner, J.E. **2004**. The nature and timing of caldera collapse as indicated by accidental lithic fragments from the AD 1000 eruption of Volcan Ceboruco, Mexico. *Journal of Volcanology and Geothermal Research*, **130**(1-2): 93-105. doi:https://doi.org/10.1016/S0377-0273(03)00283-X

Caldwell, T.G., Bibby, H.M., Brown, C. **2004**. The magnetotelluric phase tensor. *Geophysical Journal International*, **158**(2): 457-459. doi:https://doi.org/10.1111/j.1365-246X.2004.02281.x

Centro Nacional de Prevención de Desastres, CENAPRED, **2013**. Monitoreo hidrogeoquímico y térmico del Volcán Ceboruco, Subdirección de Riesgos Volcánicos, Dirección de Investigación. Ciudad de México, México. 23 pp. Available online: http://www1.cenapred.unam.mx/COORDINACION_ADMINISTRATIVA/SRM/FRACCION_XLI_A/8.pdf (In Spanish)

Centro Nacional de Prevención de Desastres, CENAPRED, **2019**. Sistema de información sobre riesgos. Available online: http://www.atlasnacionalderiesgos.gob.mx/archivo/visor-capas.html (accessed in September 2019).

Comisión Nacional del Agua, CNA, **2015**. Actualización de la disponibilidad media anual de agua en el acuífero Valle de Ixtlan Ahuacatlan (1809), Estado de Nayarit. Gerencia de Aguas Subterráneas, Comisión Nacional del Agua. Distrito Federal, Mexico. 10 pp. (In Spanish)

Chave, A.D., Thompson, D.J. **2003**. A bounded influence regression estimator based on the statistics of the hat matrix. *Journal of the Royal Statistical Society, Applied Statistics, Series C*, **52**(3): 307-323. doi:https://doi.org/10.1111/1467-9876.00406

Chave, A.D., Thompson D.J. **2004**. Bounded influence magnetotelluric response function estimation. *Geophysical Journal International*, **157**(3): 988-1006. doi:https://doi.org/10.1111/j.1365-246X.2004.02203.x

Cumming, W., Mackie, R. 2007. 3D MT resistivity imaging for geothermal resources assessment and environmental mitigation at the Glass Mountain KGRA, California. Transactions of the Geothermal Resources Council, 31: 331-334.

Díaz, D., Heise, W., Zamudio, F. 2015. Three-dimensional resistivity image of the magmatic system beneath Lastarria volcano and evidence for magmatic intrusion in the back arc (northern Chile). Geophysical Research Letters, 42(13): 5212-5218. doi:https://doi.org/10.1002/2015GL064426

Fernández-Córdoba, J., Zamora-Camacho, A., Espíndola, J.M. **2017**. Gravity Survey at the Ceboruco Volcano area (Nayarit, Mexico): a 3-D model of the subsurface structure. *Pure*

and Applied Geophysics, **174**(10): 3905-3918. doi:https://doi.org/10.1007/s00024-017-1600-4

Ferrari, L., Pasquere, G., Venegas-Salgado, S., Romero-Ríos, F. **1999**. Geology of the western Mexican Volcanic Belt and adjacent Sierra Madre Occidental and Jalisco Block. In: Delgado-Granados, H., Aguirre-Díaz, G.J., Stock, J.M. (Eds.), Cenozoic Tectonics and Volcanism of Mexico: Boulder, Colorado, Geological Society of America, Special Paper: 334 pp. doi:https://doi.org/10.1130/SPE334

Ferrari, L., Petrone C.M., Francalanci, L., Tagami, T., Eguchi, M., Conticelli, S., Manetti, P., Venegas-Salgado, S. **2003**. Geology of the San Pedro-Ceboruco Graben western Trans-Mexican Volcanic Belt. *Revista Mexicana de Ciencias Geológicas*, **20**(3): 165-181.

Ferrari, L., Valencia-Moreno, M., Bryan, S. **2007**. Magmatism and tectonics of the Sierra Madre Occidental and its relation with the evolution of the western margin of North America. In: Alaniz-Álvarez, S.A., Nieto-Samaniego, A.F. (Eds.), Geology of Mexico: Celebrating the Centenary of the Geological Society of Mexico: Geological Society of America, Special Paper: 422. doi:https://doi.org/10.1130/SPE422

Ferrari, L., Orozco-Esquivel, T., Manea, V., Manea, M. **2012**. The dynamic history of the Trans-Mexican Volcanic Belt and the Mexico subduction zone. *Tectonophysics*, **522-523**(2012): 122-149. doi:https://doi.org/10.1016/j.tecto.2011.09.018

Ferrés-López, M.D., Sieron, K., González-Zuccolotto, K., Constantinescu, R., Agustín-Flores, J., Siebe-Grabach, C., Capra-Pedol, L. Connor, L., Connor, C.B. **2019**. *Memoria técnica del mapa de peligros del volcán Ceboruco (Nayarit)*. Monografías del instituto de Geofísica, Universidad Nacional Autónoma de México, Ciudad de México, México. 182 pp.

Frey, H.M., Lange, R.A., Hall, C.M., Delgado-Granados, H. **2004**. Magma eruption rates constrained by Ar^{40}/Ar^{39} Chronology and GIS for the Ceboruco-San Pedro volcanic field, western Mexico. *Geological Society of America Bulletin*, **116**(3-4): 259-276. doi:10.1130/B25321.1

Gamble, T.D., Goubou, W.M., Clarke, J. **1979**. Magnetotellurics with a remote reference. *Geophysics*, **44**(1), 53-68. doi:https://doi.org/10.1190/1.1440923

Gardner, J.E., Tait, S. **2000**. The caldera-forming eruption of Volcan Ceboruco, Mexico. *Bulletin of Volcanology*, **62**(1): 20-33. doi:https://doi.org/10.1007/s004450050288

Gastil, R.G., Krummenacher, D., Jansky, A.W. 1978. A Reconnaissance geologic map of the west-central part of the state of Nayarit, Mexico: Geological Society of America, Map and Chart Series, MC-24, scale 1:200,000, 1 map.

Glover, P.W.J., Hole, M.J., Pous, J. 2000. A modified Archie's law for two conducting phases. Earth and Planetary Science Letters, 180(3-4): 369-383. doi:https://doi.org/10.1016/S0012-821X(00)00168-0

Hill, G.J., Caldwell, T.G., Heise, W., Chertkoff, D.G., Bibby, H.M., Burgess, M.K., Cull, J.P., Cas, R.A. **2009**. Distribution of melt beneath Mount St Helens and Mount Adams inferred from magnetotelluric data. **2009**. *Nature Geosciences*, **2**: 785-789. doi:https://doi.org/10.1038/ngeo661

Hiriart-Le Bert, G., Gutiérrez-Negrín, L.C.A., Quijano-León, J.L., Ornelas-Celis, A., Espíndola, S., Hernández, I. **2011**. Evaluación de la Energía Geotérmica en México, *Informe para el Banco Interamericano de Desarrollo y la Comisión Reguladora de Energía*, Ciudad de México, México. 167 pp. Available online: http://www.cre.gob.mx/documento/2026.pdf (In Spanish)

Ingham, M.R., Bibby, H.M., Heise, W., Jones, K.A., Cairns, P., Dravitzki, S., Bennie, S.L., Caldwell, T.G., Ogawa, Y. **2009**. A magnetotelluric study of Mount Ruapehu volcano, New Zealand. *Geophysical Journal International*, **179**(2): 887-904. doi:https://doi.org/10.1111/j.1365-246X.2009.04317.x

Instituto Nacional de Estadística y Geografía, INEGI, **2019**. Mapa Digital de México. Available online: http://gaia.inegi.org.mx/mdm6/ (accessed on September 2019).

Kelbert, A., Meqbel, N., Egbert, G.D., Tandon, K. **2014**. ModEM: A modular system for inversion of electromagnetic geophysical data. *Computer and Geosciences*, **66**: 40-53. doi:https://doi.org/10.1016/j.cageo.2014.01.010

Laumonier, M., Gaillard, F., Sifre, D. 2015. The effect of pressure and water concentration on the electrical conductivity of dacitic melts: Implication for magnetotelluric imaging in subduction areas. Chemical Geology, 418: 66-76. doi:https://doi.org/10.1016/j.chemgeo.2014.08.019

Laumonier, M., Gaillard, F., Muir, D., Blundy, J., Unsworth, M. 2017. Giant magnetic water reservoirs at mid-crustal depth inferred from electrical conductivity and growth of the continental crust. Earth and Planetary Science Letters, 457: 173-180. doi:https://doi.org/10.1016/j.epsl.2016.10.023

Luhr, J.F. 1992. Slab-derived fluids and partial melting in subduction zones: insights from two contrasting Mexican volcanoes (Colima and Ceboruco). Journal of Volcanology and Geothermal Research, 54(1-2): 1-18. doi:https://doi.org/10.1016/0377-0273(92)90111-P

Mancini, R., Díaz, D., Brasse, H., Godoy, B., Hernández, J.M. 2019. Conductivity distribution beneath the San Pedro-Linzor volcanic chain, North Chile, using 3-D magnetotelluric modeling. Journal of Geophysical Research, Solid Earth, 124(5): 4386-4398. doi:https://doi.org/10.1029/2018JB016114

Matsushima, N., Utsugi, M., Takakura, S., Yamasaki, T., Hata, M., Hashimoto, T., Uyeshima, M. **2020**. Magmatic-hydrothermal system of Aso volcano, Japan, inferred from electrical resistivity structures. *Earth, Planet, and Space*. **72**(57). doi:https://doi.org/10.1186/s40623-020-01180-8

McDowell, F.W., Clabaugh, S.E. **1979**. Ignimbrites of the Sierra Madre Occidental and their relation to the tectonic history of western Mexico. *Geological Society of America, Special Paper*, 180: 113-124. doi:https://doi.org/10.1130/SPE180-p113

Moore, J.N., Allis, R.G., Nemcok, M., Powell, T.S., Bruton, C.J., Wannamaker, P.E., Raharjo, I.B., Norman, D.I. **2008**. The evolution of the volcano-hosted geothermal systems based on deep wells from Karaha-Telega Bodas, Indonesia. *American Journal of Sciences*, **308**(1): 1-48. doi:https://doi.org/10.2475/01.2008.01

Muñoz, G. 2014. Exploring for geothermal resources with electromagnetic methods. Surveys in Geophysics, 35(1): 101-122. doi:https://doi.org/10.1007/s10712-013-9236-0

Nelson, S.A. **1980**. Geology and petrology of Volcan Ceboruco, Nayarit, Mexico. *Geological Society of America Bulletin*, **91**(11, Part II): 2290-2431. doi:https://doi.org/10.1130/GSAB-P2-91-2290

Nelson, S.A. **1986**. Geología del Volcán Ceboruco, con una estimación de riesgos de erupciones futuras. *Revista Mexicana de Ciencias Geológicas*, **6**: 243-258.

Núñez-Cornú, F.J., Escalona-Alcázar, F.J., Núñez-Escribano, D., Trejo-Gómez, E., Suárez-Plascencia, C., Rodríguez-Ayala, N. **2020**. Study of seismic activity at Ceboruco Volcano (Nayarit, Mexico) in the period 2012 to 2014. *Journal of South American Earth Sciences*, **98**. doi:https://doi.org/10.1016/j.jsames.2019.102473

Pellerin, L., Johnston, J.M., Hohmann, G.W. **1996**. A numerical evaluation of electromagnetic methods in geothermal exploration. *Geophysics*, **61**(1): 121-130. doi:https://doi.org/10.1190/1.1443931

Petrone, C.M., Tagami, T., Francalanci, L., Matsumara, A., Sudo, M. **2001**. Volcanic systems in the San Pedro-Ceboruco graben (Nayarit, Mexico) in the light of new K-Ar geochronological data. *Geochemical Journal*, **35**(2): 77-88. doi:https://doi.org/10.2343/geochemj.35.77

Pommier, A., Le-Trong, E. 2011. SIGMELTS: A web portal for electrical conductivity calculations in geosciences. Computer & Geosciences, 37(9): 1450-1459. doi:https://doi.org/10.1016/j.cageo.2011.01.002

Pritchard, M.E., de Silva, S.L., Michelfelder, G., Zandt, G., McNutt, S.R., Gottsman, J., West, M.E., Blundy, J., Christensen, D.H., Finnegan, N.J., Minaya, E., Sparks, R.S.J., Sunagua, M., Unsworth, M.J., Alvizuri, C., Comeau, M.J., del Potro, R., Diaz, D., Diez, M., Farrell, A., Henderson, S.T., Jay, J.A., Lopez, T., Legrand, D., Naranjo, J.A., McFarlin, H., Muir, D., Perkins, J.P., Spica, Z., Wilder, A., Ward, K.M. 2018. Synthesis: PLUTONS: Investigating the relationship between plutons growth and volcanism in the Central Andes. Geosphere, 14(3): 954-982. doi https://doi.org/10.1130/GES01578.1

Righter, K., Carmichael, I.S.E., Becker, T. **1995**. Pliocene-Quaternary faulting and volcanism at the intersection of the Gulf of California and the Mexican Volcanic Belt. *Geological Society of America Bulletin*, **107**(6): 612-627. doi:https://doi.org/10.1130/0016-7606(1995)107<0612:PQVAFA>2.3.CO;2

Rodríguez-Uribe, M.A., Núñez-Cornú, F.J., Nava-Pichardo, F.A., Suárez-Plascencia, C. **2013**. Some insights about the activity of the Ceboruco Volcano (Nayarit, Mexico) from recent seismic low-frequency activity. *Bulletin of Volcanology*, **75**: 755. doi:https://doi.org/10.1007/s00445-013-0755-9

Sánchez, J.J., Núñez-Cornú, F.J., Suárez-Plascencia, C., Trejo-Gómez, E. **2009**. Seismicity at Ceboruco Volcano, Mexico. *Seismological Research Letters*, **80**(5): 823-830. doi:https://doi.org/10.1785/gssrl.80.5.823

Sawires, R., Aboud, E. **2019**. Subsurface structural imaging of Ceboruco Volcano area, Nayarit, Mexico, using high-resolution aeromagnetic data. *Journal of Volcanology and Geothermal Research*, **371**: 162-176. doi:https://doi.org/10.1016/j.jvolgeores.2019.01.012

Servicio Geológico Mexicano, SGM, **2019**. GEOINFOMEX, Available online: https://www.sgm.gob.mx/GeoInfoMexGobMx/ (accessed in September 2019)

Shinohara, H. **1994**. Exsolution of immiscible vapor and liquid phases from a crystallizing silicate melt: Implications for chlorine and metal transport. *Geochemica et Cosmochimica Acta*, **58**(23): 5215-5221. doi:https://doi.org/10.1016/0016-7037(94)90306-9

Sieron, K., C. Siebe. **2008**. Revised stratigraphy and eruption rates of Ceboruco stratovolcano and surrounding monogenetic vents (Nayarit, Mexico) from historical documents and new radiocarbon date. *Journal of Volcanology and Geothermal Research*, **176**(2): 241-264. doi:https://doi.org/10.1016/j.jvolgeores.2008.04.006

Spichak, V., Manzella, A. 2009. Electromagnetic sounding of geothermal zones. Journal of Applied Geophysics, 68(4): 459-478. doi:https://doi.org/10.1016/j.jappgeo.2008.05.007

Stock, J.M. **1993**. Tectónica de placas y evolución del Bloque Jalisco, México. *GEOS, Boletín de la Unión Geofísica Mexicana*, **13**(3): 3-9.

Suárez-Plascencia, C. **1998**. Análisis de las variables del riesgo volcánico en el volcán Ceboruco, Nayarit, México. Tesis de Maestría en Ciencias. Centro de Investigación Científica y de Educación Superior de Ensenada. Ensenada, Baja California, México. 146 pp. (In Spanish)

Tello-Hinojosa, E. **1994**. Geochemistry of the thermal springs around the Ceboruco Volcano, Nayarit, Mexico. *Geotermia, Revista Mexicana de Geoenergia*, **10**(2): 3-8. (In Spanish)

Unsworth M., Rondenay, S. 2013. Mapping the Distribution of Fluids in the Crust and Lithospheric Mantle Utilizing Geophysical Methods. In: Metasomatism and the Chemical Transformation of Rock. Lecture Notes in Earth System Sciences. Springer, Berlin, Heidelberg. doi:https://doi.org/10.1007/978-3-642-28394-9_13

Ussher, G., Harvey, C., Johnstone, R., Anderson, E. 2000. Understanding the resistivities observed in geothermal systems. In: Proceedings World Geothermal Congress, Kyushu-Tohoku, Japan, 2000. 1915-1920.

Valencia, V.A., Righter, K., Rosas-Elguera, J., López-Martínez, M., Grove, M. **2013**. The age and composition of the pre-Cenozoic basement of the Jalisco Block: implications for and relation to the Guerrero composite terrane. *Contributions to Mineralogy and Petrology*, **166**: 801-824. doi:https://doi.org/10.1007/s00410-013-0908-z

Venegas, S. **1995**. Geothermal exploration results at the Ceboruco Volcano, Nayarit State, Mexico. *Geotermia, Revista Mexicana de Geoenergía*, **11**(2): 71-86. (In Spanish).

Viggiano-Guerra, J.C. **1993**. Conceptual model at the Ceboruco volcano geothermal reservoir: An approach. *Geotermia, Revista Mexicana de Geoenergia*, **9**(3): 369-388. (In Spanish)

Wright, P.M., Ward, S.H., Ross, H.P., West, R.C. **1985**. State of the art geophysical exploration for geothermal resources. *Geophysics*, **50**(12): 2666-2696. doi:https://doi.org/10.1190/1.1441889

Tables

Table (1). Sampling frequency recorded at each MT-Station.

Sampling rate [Hz]	ID-Magnetotelluric Station
32768	CB01, CB03, CB04, CB05, CB06, CB07, CB12, CB15, CB20, CB21, CB22, CB23, CB24, CBF1, CBF3, CBF5, CB02*, CB08*, CB11*, CB14*, CB16*, CB17*, CB18*, CBF2*
2048	CB01, CB03, CB04, CB05, CB06, CB07, CB12, CB20, CB21, CB22, CB23, CBF3, CB14*, CB17*, CB18*, CBF2
512	CB01, CB04, CB06, CB07, CB12, CB20, CB21, CB23, CBF3, CBF5
128	CB03, CB05, CB22

Note: MT-Stations denoted with (*) were not considered in this study.

Figure Captions

Figure (1). Location map of Ceboruco Volcano showing its spatial relation to the surrounding tectonic domains and plate boundaries. Filled black triangles showed principal volcanoes of the Trans-Mexican Volcanic Belt (CENAPRED, 2019). Rift zones: Tepic-Zacoalco (TZR), Chapala (ChaR), and Colima (ColR) also are indicated. Gray solid-line shows the tectonic-fault systems (Ferrari et al., 2012). Star symbols show the largest regional cities: Guadalajara (GDL), Tepic (TEP), and Colima (COL). Inset: Location map of the study area within Mexico. Geographical coordinate system, datum WGS84.

Figure (2). Regional-local geologic map of the San Pedro-Ceboruco Graben. Exploration-gradient wells, lava-cinder cones (Ferrari et al., 2003). Faults and lithology (Ferrari et al., 2012; SGM, 2019; INEGI; 2019). Universal Transverse Mercator coordinate system, datum WGS84.

Figure (3). a) Detailed representation of the volcanic deposits erupted by Ceboruco Volcano (Sieron and Siebe, 2008; CENAPRED, 2019). b) Stratigraphy of the in-depth exploration well CB-1 drilled by the Federal Electricity Commission at the southern foothills of Ceboruco Volcano (Modified after Ferrari et al., 2003). Please note that each lithological unit's elevation is reported in meters sea level (m.s.l.). Additionally, depth concerning terrain surface is indicated.

Figure (4). Location of magnetotelluric stations on and around Ceboruco Volcano. The MT-3D profiles are also illustrated. The main hydrogeological features are shown (For

interpretation of these features, the reader is referred to the Figure 1 Supplementary Material).

Figure (5). Example of the curves at four representative MT-Stations (CB01, CB23, CB24, and CBF3) observed in this study showing the apparent resistivity and phase of ZXY, ZYX impedance tensor components. Transfer functions computed for the four impedance tensor components at 16 MT-Station are shown in Figure 2 of Supplementary Material.

Figure (6). Phase-tensor ellipses at four periods (0.01, 1, 10, and 100 s) at all MT-Stations. The color scale is indicating the beta-angle value.

Figure (7). Profiles extracted from the 3D inversion model. The location of each MT-profiles is shown in Figure 4. Please note that the geoelectrical features (R1, R2, R2, C1, C2, C3) are described in the main text. In addition, note that S.L.A. and S.L.B. correspond to structural lineaments inferred from epicentral distributions proposed by Núñez-Cornú et al. (2020). IF-CE-NW indicates the buried inferred fault associated with the WNW trending alignment of cinder cones and lava domes reported by Ferrari et al. (2003). The water table elevation of the regional aquifer is denoted with a dashed line and marked as WL.

Figure (8). Schematic representation of the interpreted geothermal reservoir beneath Ceboruco Volcano from 3D inversion-modeling of magnetotelluric data and their relation with the conceptual model proposed by Venegas (1995).

Figure (9). Archie's law plotted as bulk resistivity vs. melt fraction (left) and porosity (right); in both cases, a value of 1.50 for the cementation coefficient was used. a) Prediction model of the fraction melting based on the resistivity values estimated using Sigmelts considering rock composition, pressure, temperature, and water content for a felsic model (solid lines) and an intermediate model (dashed lines). b) Prediction model of bulk resistivity from a mix of hypothetical brines (1.00, 0.10, and 0.10 Ωm) contained in rock porous-phase. At both graphs, horizontal black lines represent the resistivities obtained for 3D inversion modeling.

Figure (1), Supplementary Material. Hydrogeological and seismicity setting. Epicentral locations reported by Núñez-Cornú et al. (2020). Main hydrogeological features based on (CENAPRED, 2015; INEGI, 2019).

Figure (2), Supplementary Material. Transfer functions obtained after robust processing the time series recorded at 16 MT-Sites considering the four impedance tensor components.

Figure (3), Supplementary Material. The apparent resistivity and phase of ZXY, ZYX impedance tensor components at 16 MT-Stations. The blue and red circles with error bars show the XY and YX observed data. The solid lines show the inversion response of the preferred 3D inversion model.

Figure (4), Supplementary Material. Comparative maps are showing station locations colored by the RMS misfit ratio as a result of sensitivity tests. The final inversion model RMS misfit distribution is denoted as MInv. RMS misfit related to the model that was replacing the resistivity to 100 Ωm is indicated as SAM1. RMS misfit associated with

simulating and elongate-vertical shape is marked as SAM3. RMS misfit computed from the model that tests the connection between C1 and C2 is denoted as SAM2.

Figure (1). Location map of Ceboruco Volcano showing its spatial relation to the surrounding tectonic domains and plate boundaries. Filled black triangles showed principal volcanoes of the Trans-Mexican Volcanic Belt (CENAPRED, 2019). Rift zones: Tepic-Zacoalco (TZR), Chapala (ChaR), and Colima (ColR) also are indicated. Gray solid-line shows the tectonic-fault systems (Ferrari et al., 2012). Star symbols show the largest regional cities: Guadalajara (GDL), Tepic (TEP), and Colima (COL). Inset: Location map of the study area within Mexico. Geographical coordinate system, datum WGS84.

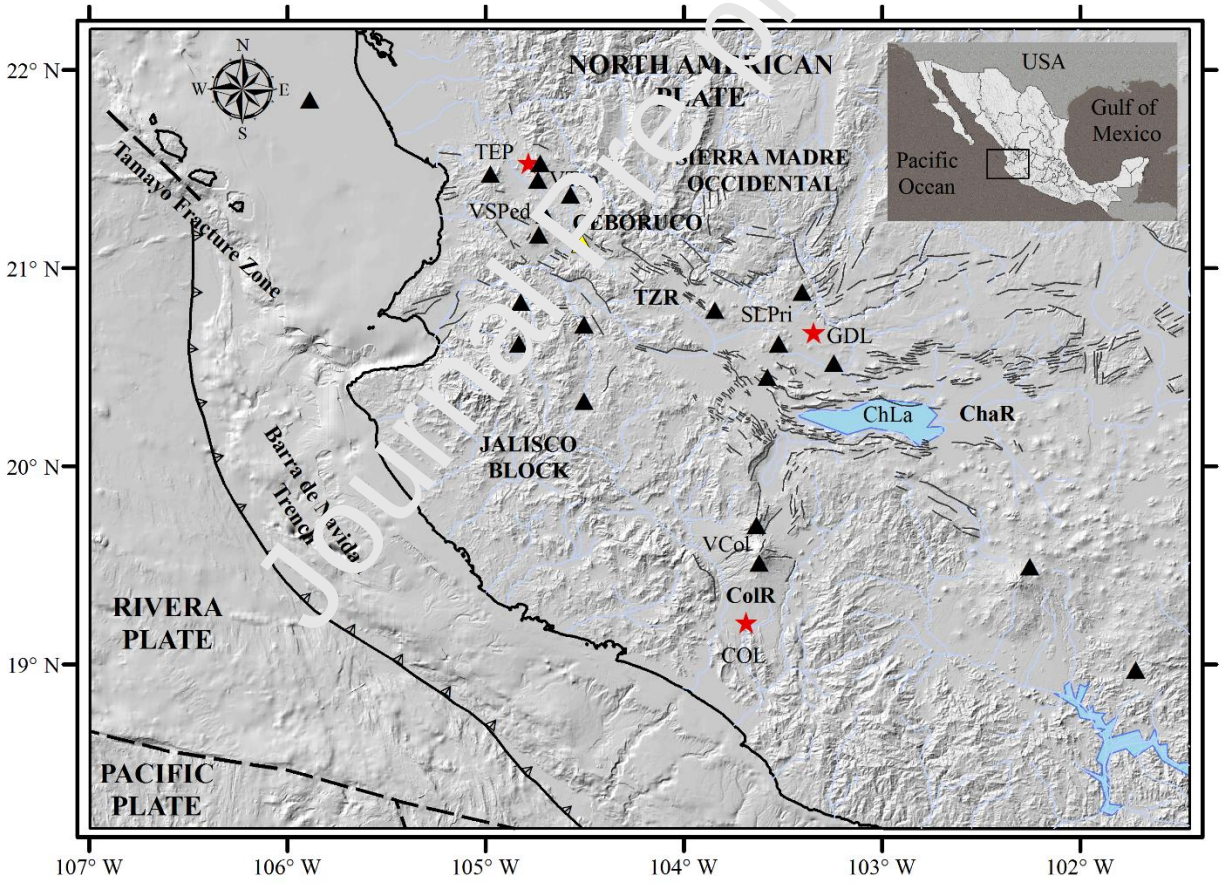

Figure (2). Regional-local geologic map of the San Pedro-Ceboruco Graben. Exploration-gradient wells, lava-cinder cones (Ferrari et al., 2003). Faults and lithology (Ferrari et al., 2012; SGM, 2019; INEGI; 2019). Universal Transverse Mercator coordinate system, datum WGS84.

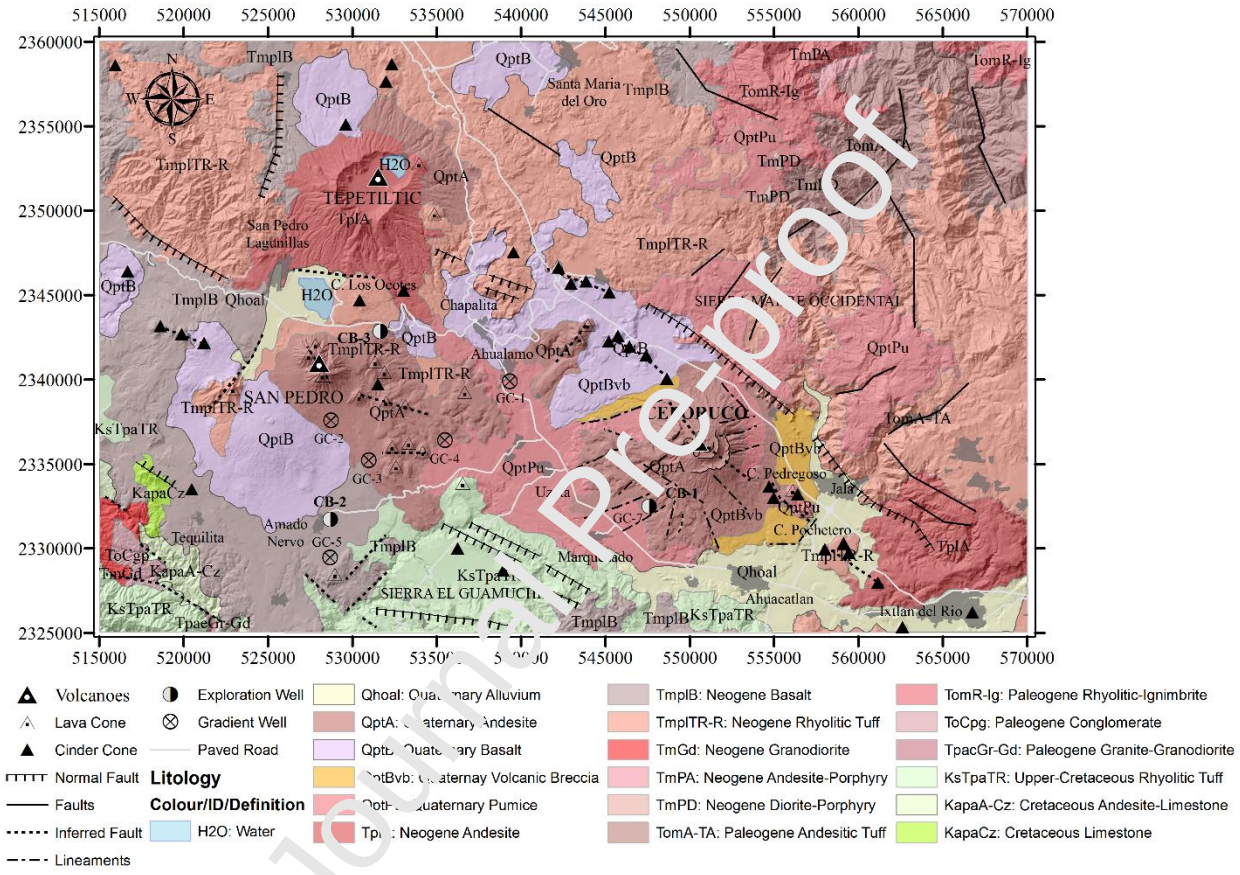

Figure (3). a) Detailed representation of the volcanic deposits erupted by Ceboruco Volcano (Sieron and Siebe, 2008; CENAPRED, 2019). b) Stratigraphy of the in-depth exploration well CB-1 drilled by the Federal Electricity Commission at the southern foothills of Ceboruco Volcano (Modified after Ferrari et al., 2003). Please note that each lithological unit's elevation is reported in meters sea level (m.s.l.). Additionally, depth concerning terrain surface is indicated.

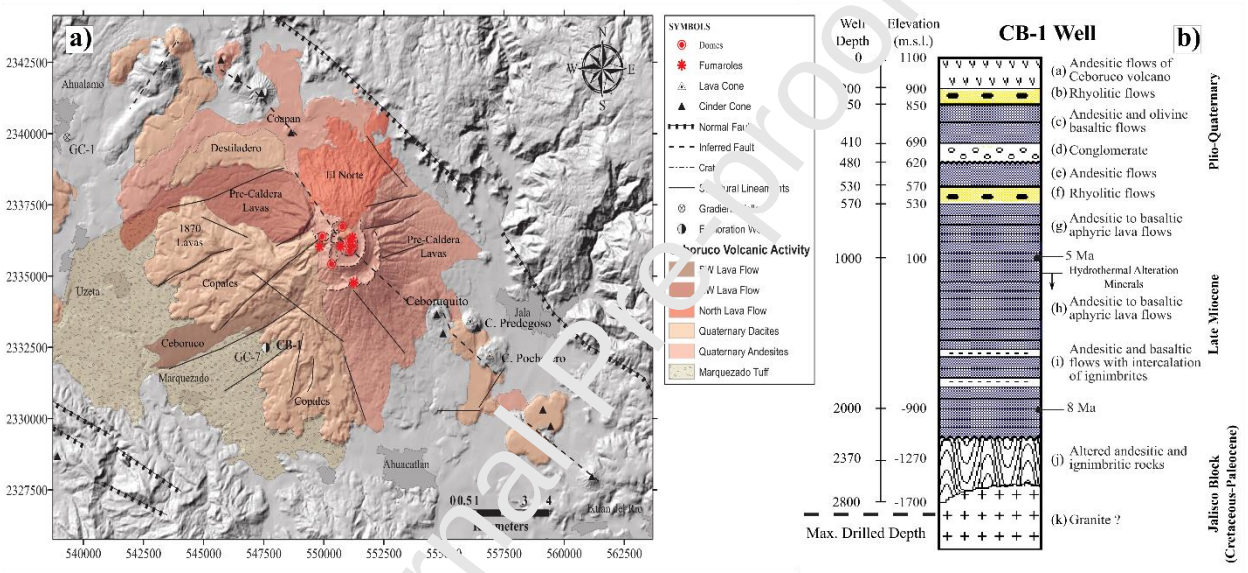

Figure (4). Location of magnetotelluric stations on and around Ceboruco Volcano. The MT-3D profiles are also illustrated. The main hydrogeological features are shown (For interpretation of these features, the reader is referred to the Figure 1 Supplementary Material online version).

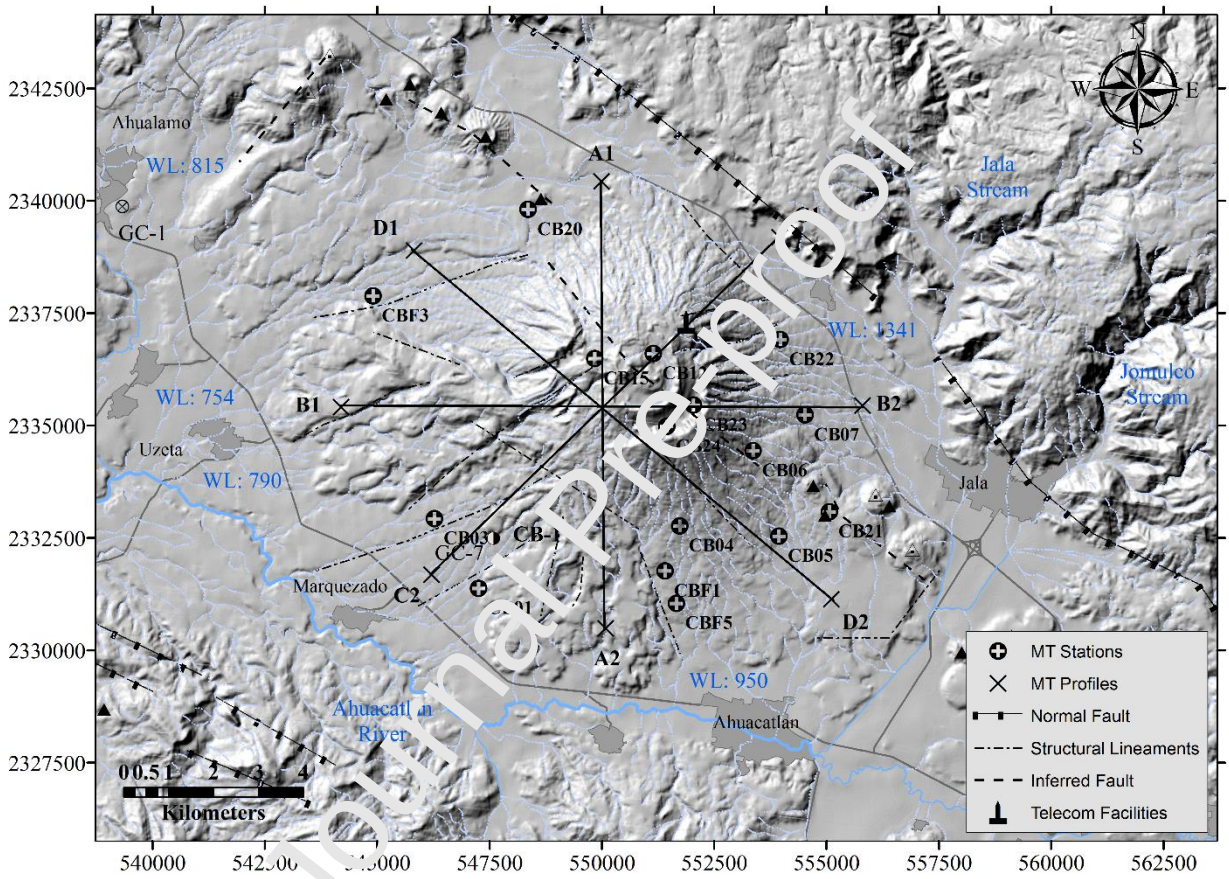

Figure (5). Example of the curves at four representative MT-Stations (CB01, CB23, CB24, and CBF3) observed in this study showing the apparent resistivity and phase of Z_{XY}, Z_{YX} impedance tensor components. Transfer functions computed for the four impedance tensor components at 16 MT-Station are shown in Figure 2 of Supplementary Material.

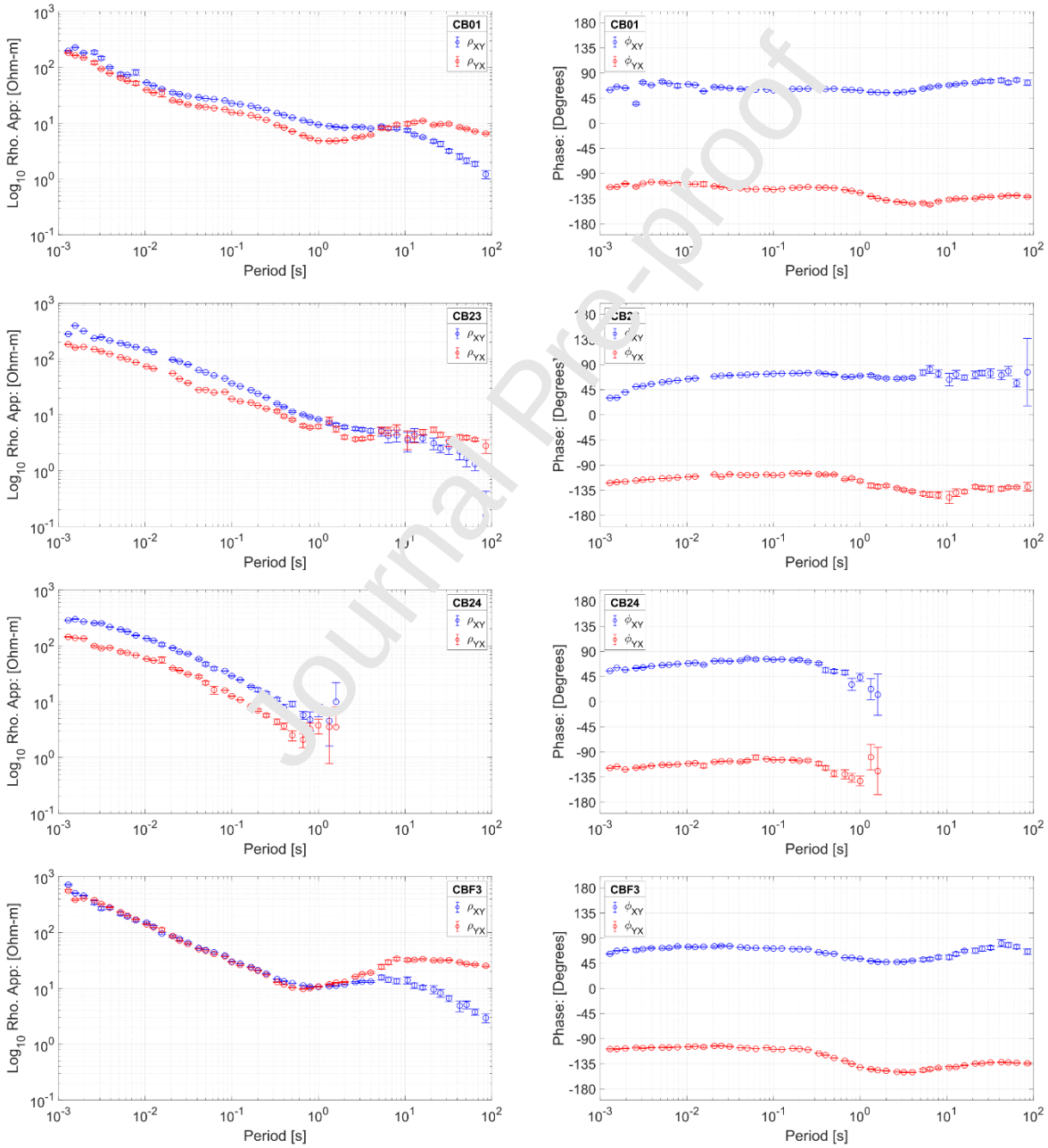

Figure (6). Phase-tensor ellipses at four periods (0.01, 1, 10, and 100 s) at all MT-Stations. The color scale is indicating the beta-angle value.

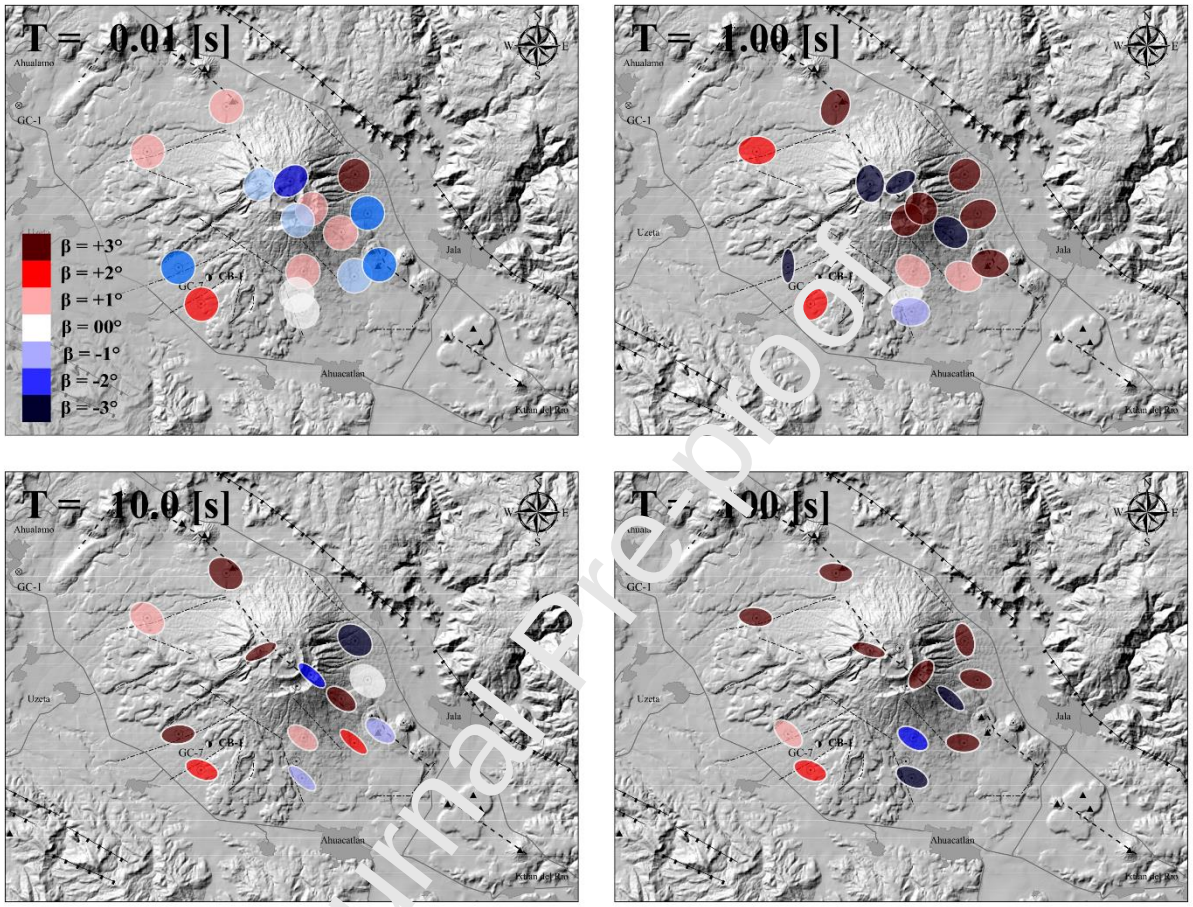

Figure (7). Profiles extracted from the 3D inversion model. The location of each MT-profiles is shown in Figure 4. Please note that the geoelectrical features (R1, R2, R2, C1, C2, C3) are described in the main text. In addition, note that S.L.A. and S.L.B. correspond to structural lineaments inferred from epicentral distributions proposed by Núñez-Cornú et al. (2020). IF-SE-NW indicates the buried inferred fault associated with the WNW trending alignment of cinder cones and lava domes reported by Ferrari et al. (2003). The water table elevation of the regional aquifer is denoted with a dashed line and marked as WL.

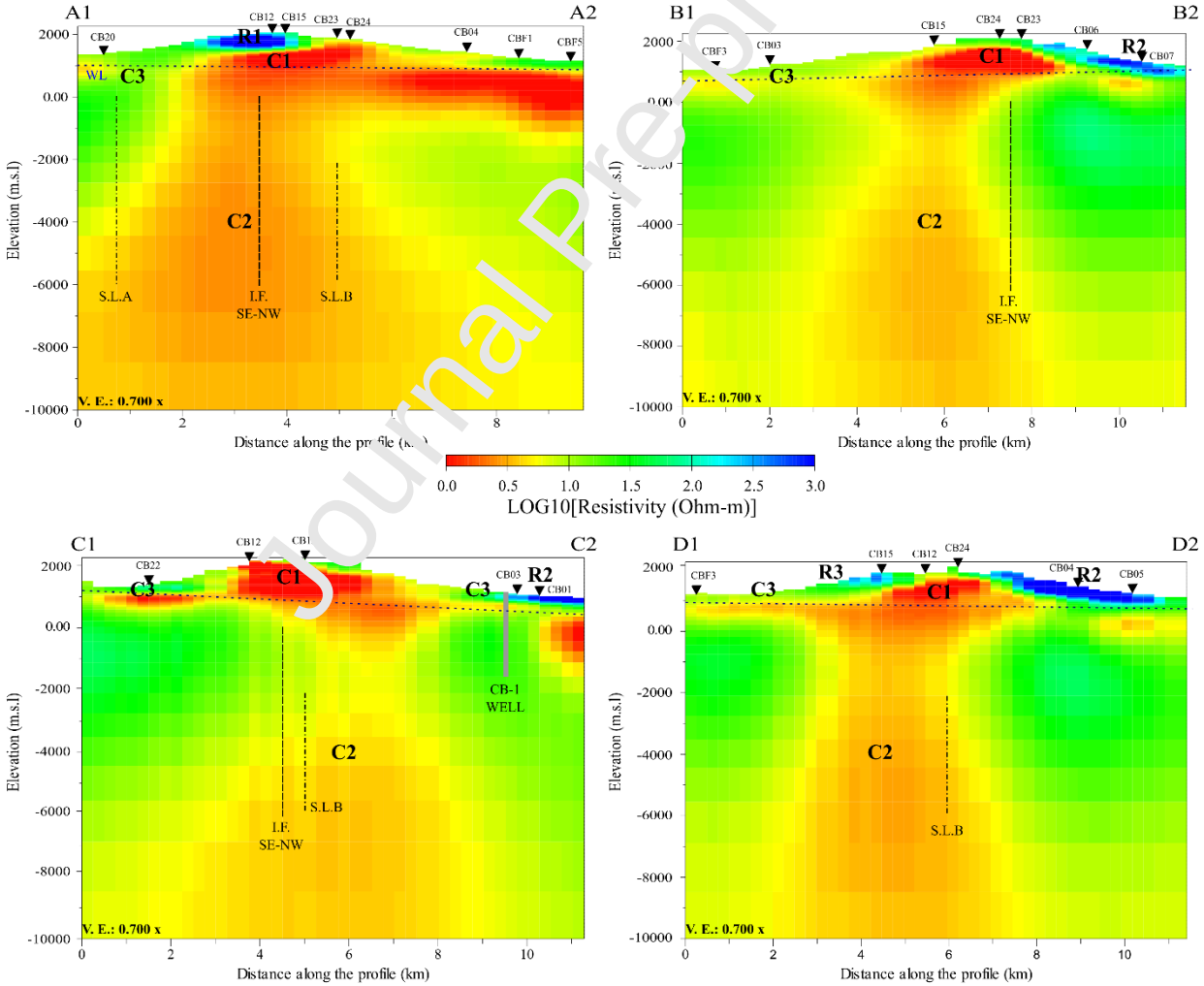

Figure (8). Schematic representation of the interpreted geothermal reservoir beneath Ceboruco Volcano from 3D inversion-modeling of magnetotelluric data and their relation with the conceptual model proposed by Venegas (1995).

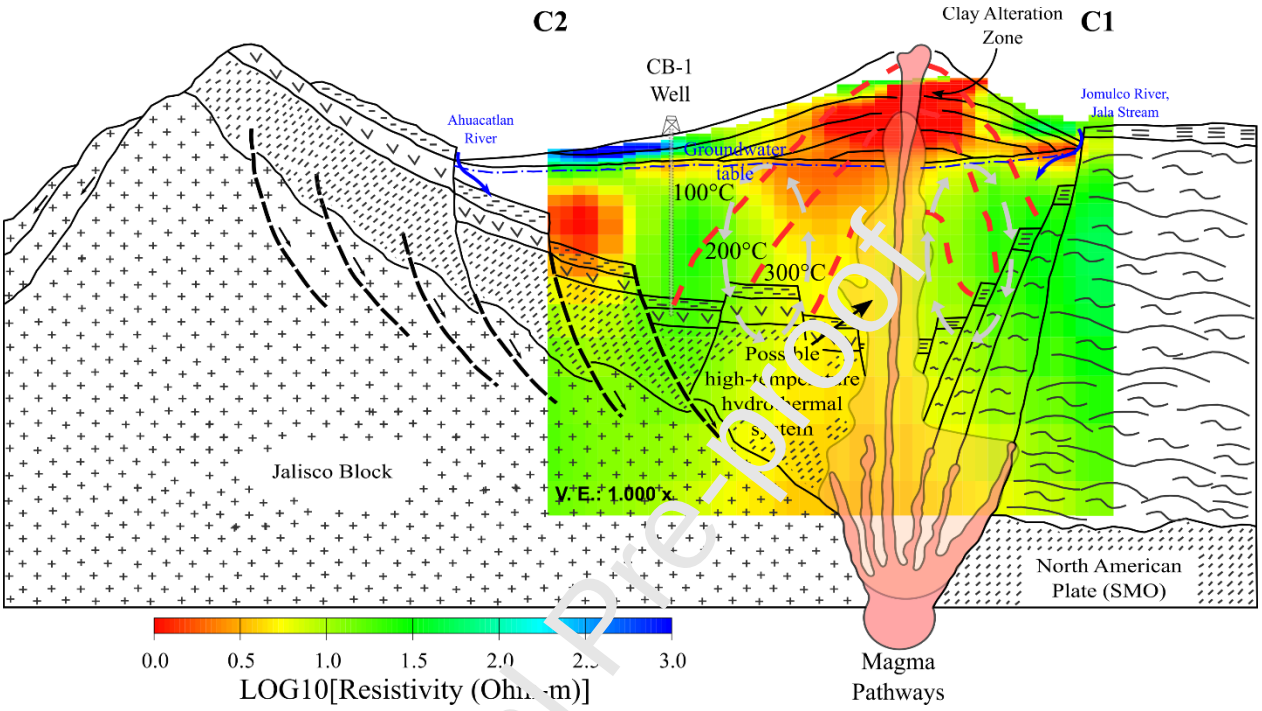

Figure (9). Archie's law plotted as bulk resistivity vs. melt fraction (left) and porosity (right); in both cases, a value of 1.50 for the cementation coefficient was used. a) Prediction model of the fraction melting based on the resistivity values estimated using Sigmelts considering rock composition, pressure, temperature, and water content for a felsic model (solid lines) and an intermediate model (dashed lines). b) Prediction model of bulk resistivity from a mix of hypothetical brines (1.00, 0.10, and 0.10 Ωm) contained in rock porous-phase. At both graphs, horizontal black lines represent the resistivities obtained for 3D inversion modeling.

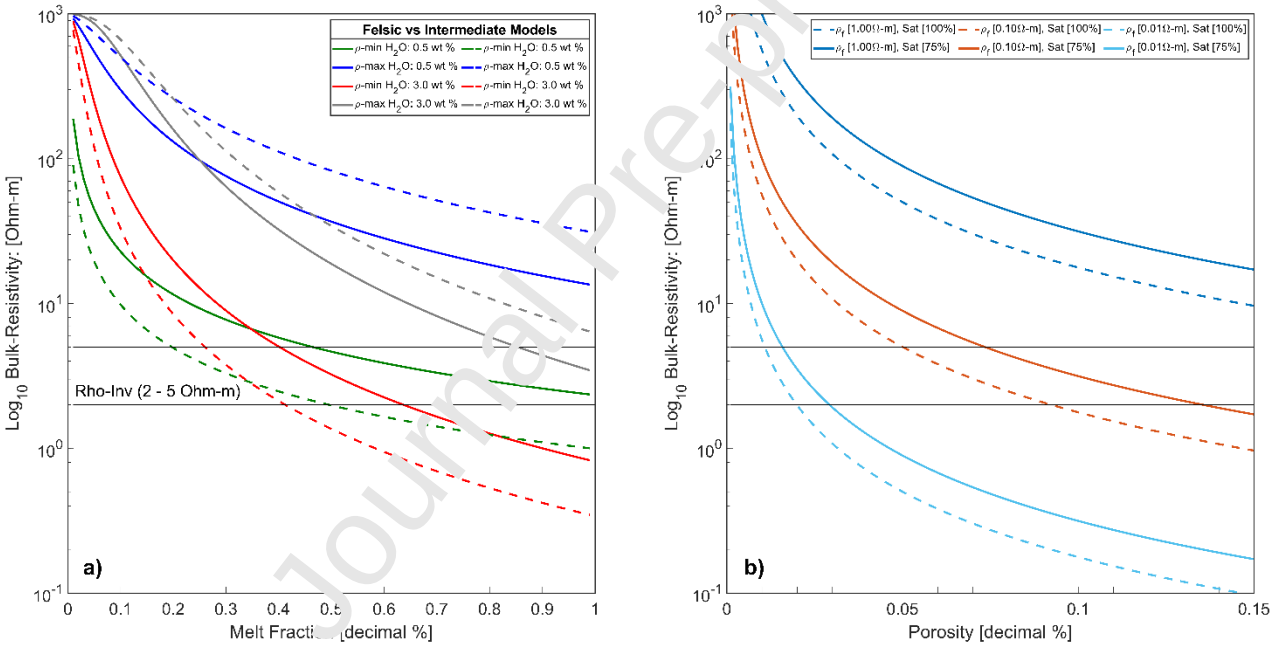

Figure (1), Supplementary Material. Hydrogeological and seismicity setting. Epicentral locations reported by Núñez-Cornú et al. (2020). Main hydrogeological features based on (CENAPRED, 2015; INEGI, 2019).

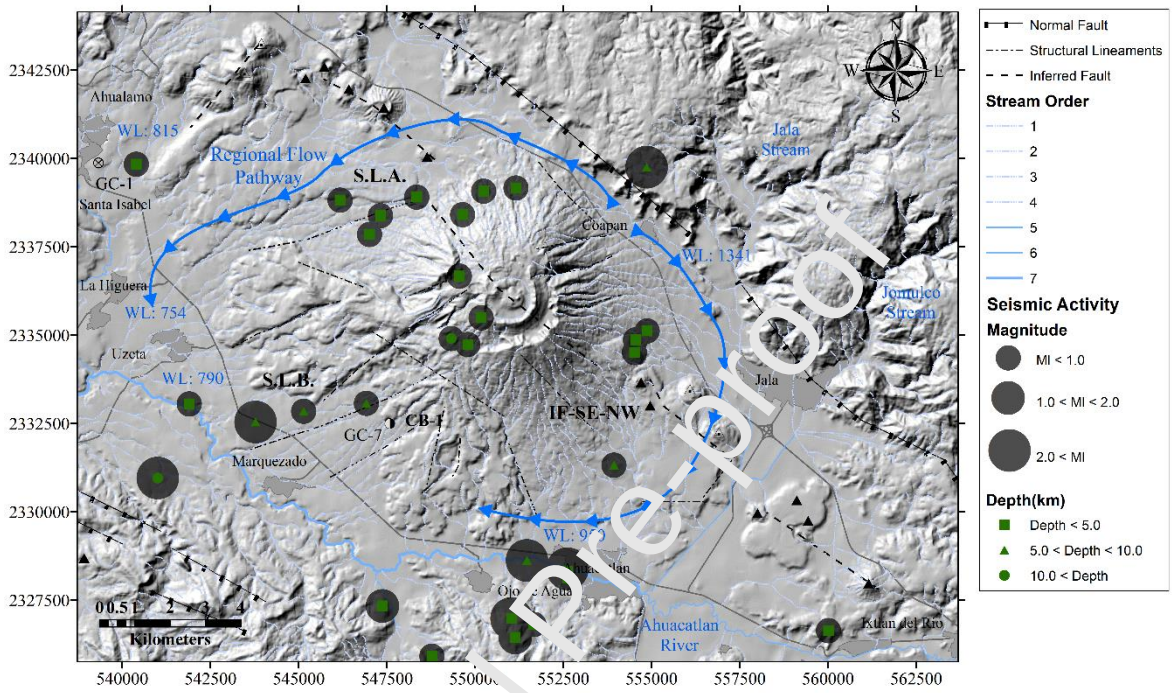

Figure (2), Supplementary Material. Transfer functions obtained after robust processing the time series recorded at 16 MT-Sites considering the four impedance tensor components.

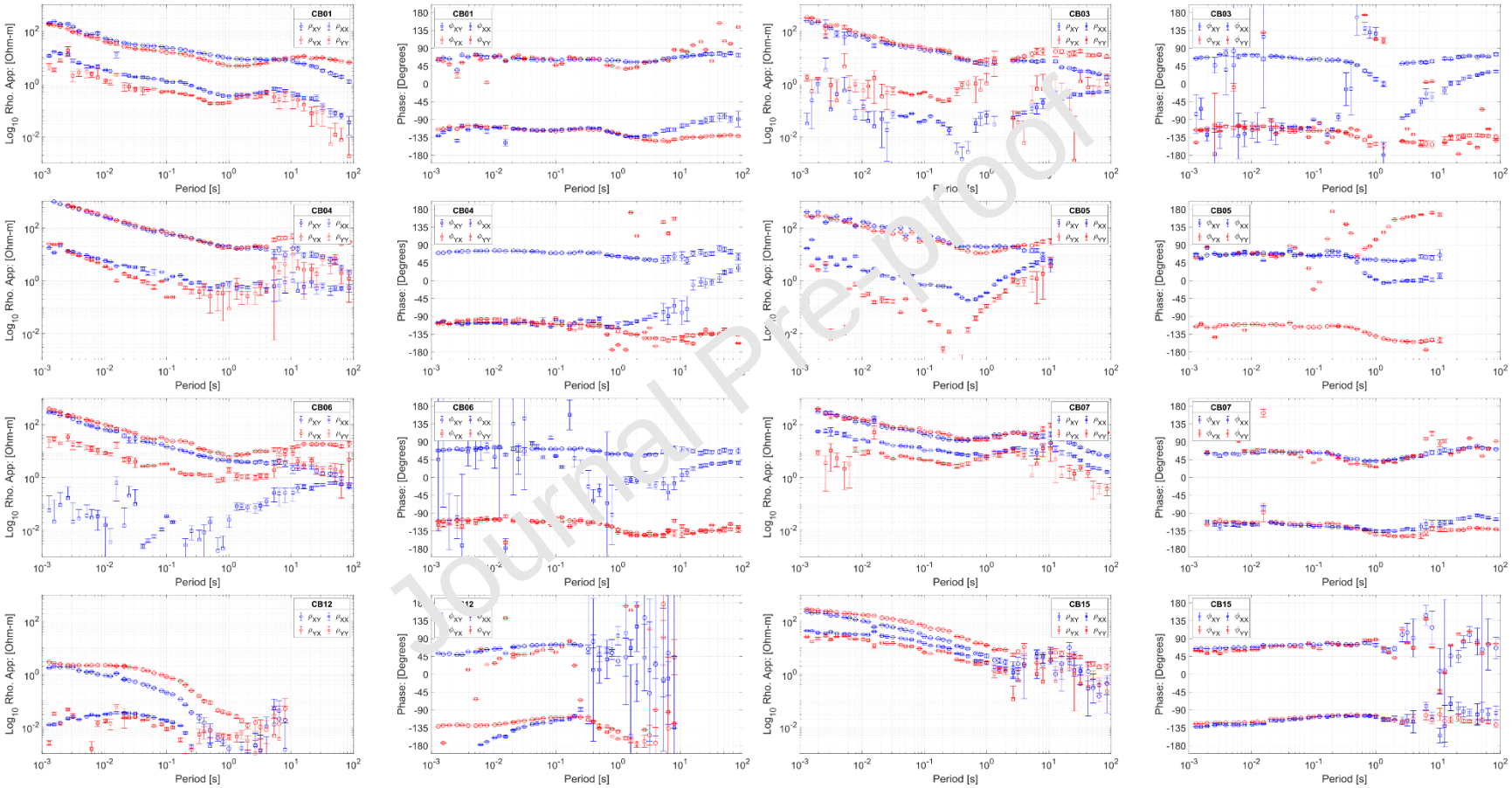

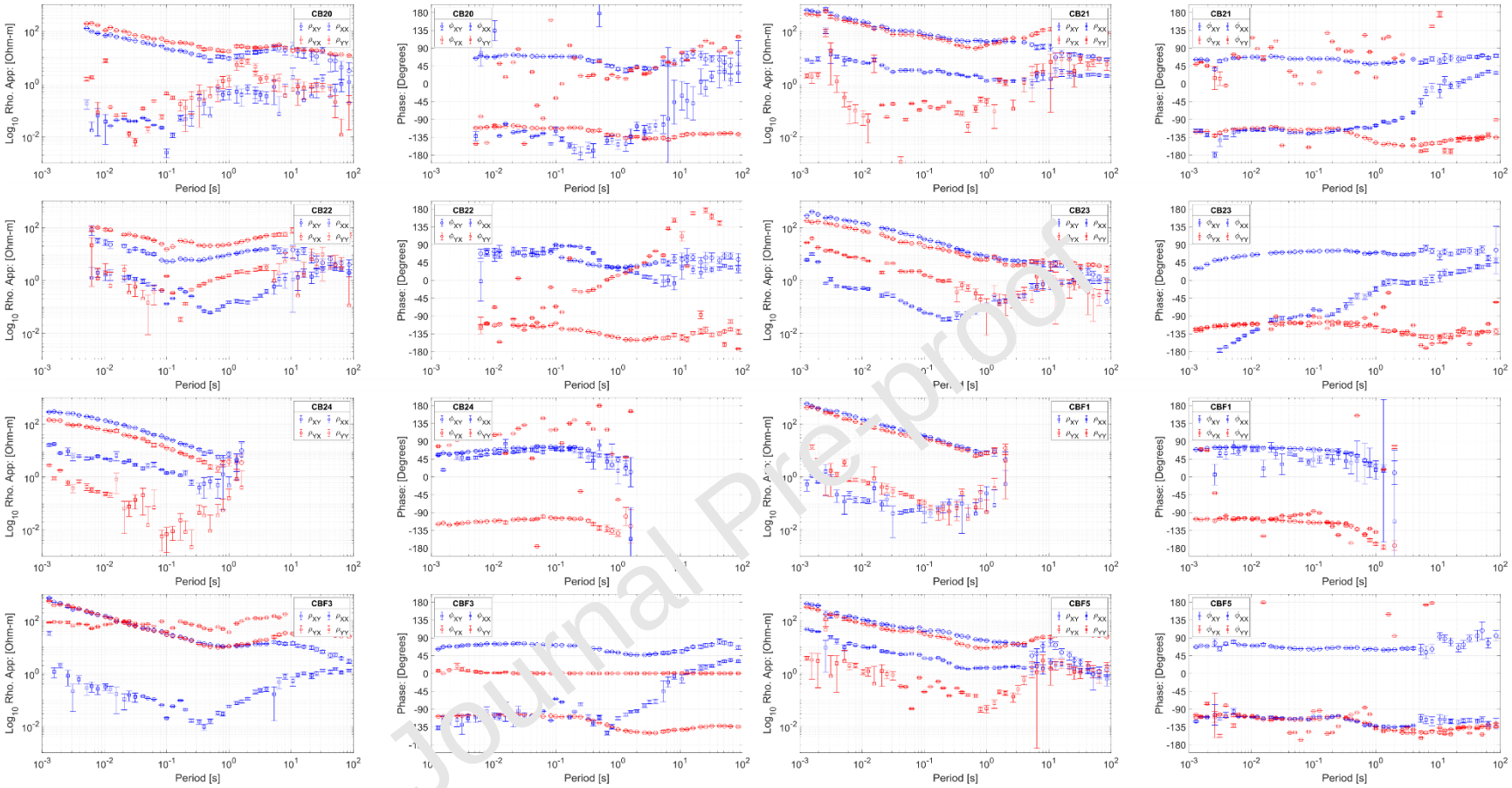

Figure 03, Supplementary Material:

The apparent resistivity and phase of ZXY, ZYX impedance tensor components at 16 MT-Stations. The blue and red circles with error bars show the XY and YX observed data. The solid lines show the inversion response of the preferred 3D inversion model.

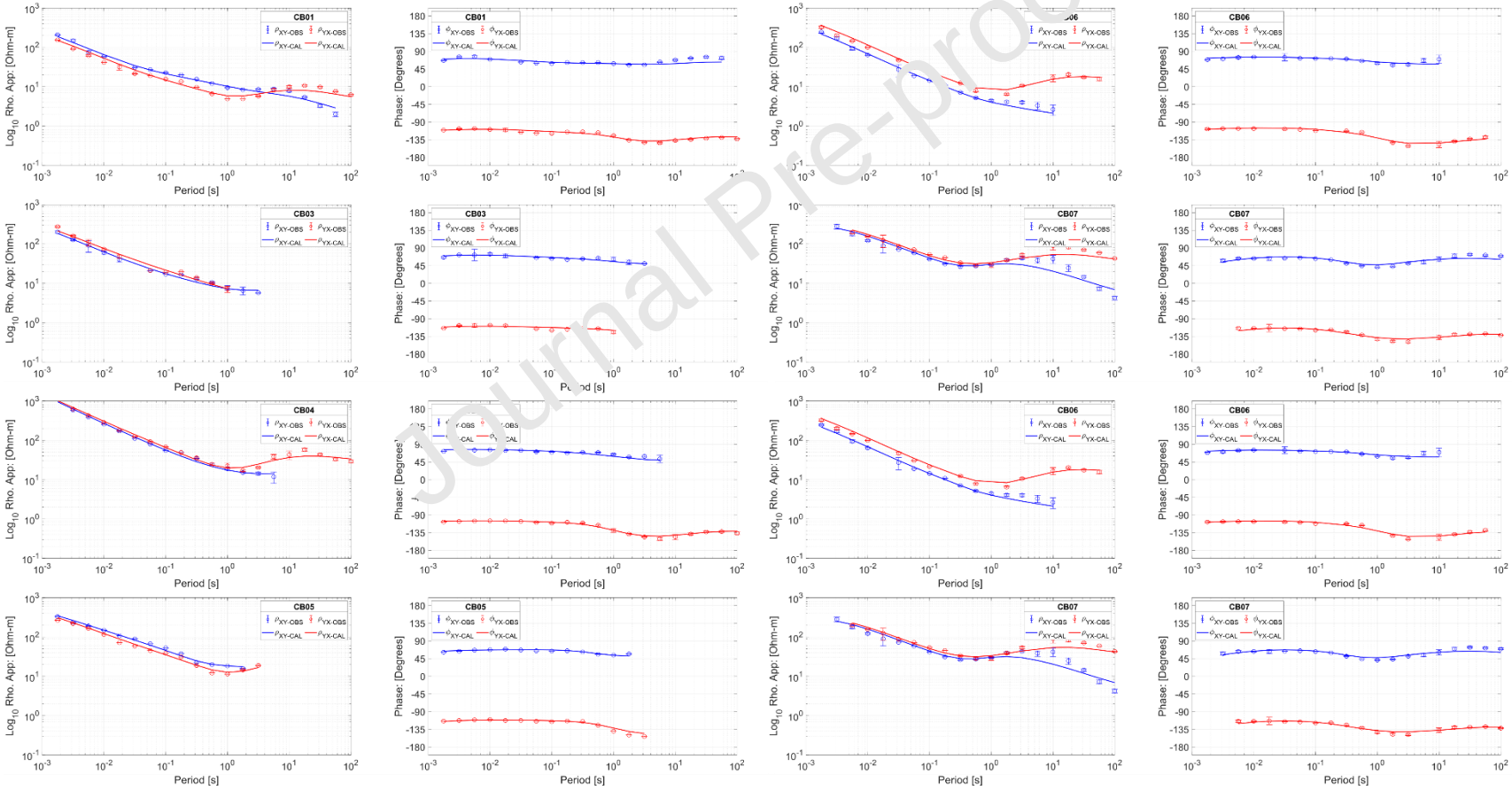

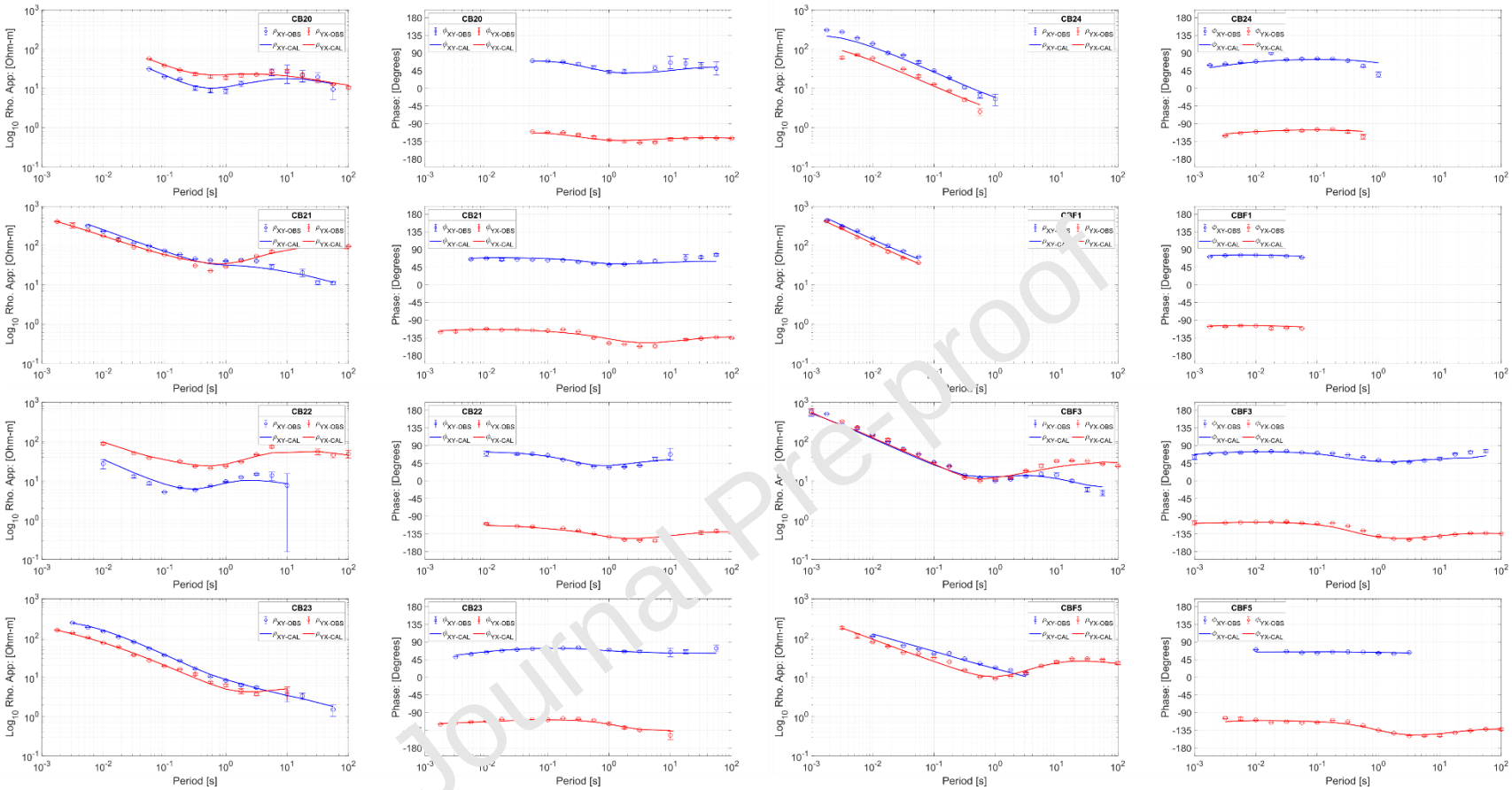

Figure 03, Supplementary Material:

Comparative maps are showing station locations colored by the RMS misfit ratio as a result of sensitivity tests. The final inversion model RMS misfit distribution is denoted as MInv. RMS misfit related to the model that was replacing the resistivity to 100 Ωm is indicated as SAM1. RMS misfit associated with simulating and elongate-vertical shape is marked as SAM3. RMS misfit computed from the model that tests the connection between C1 and C2 is denoted as SAM2.

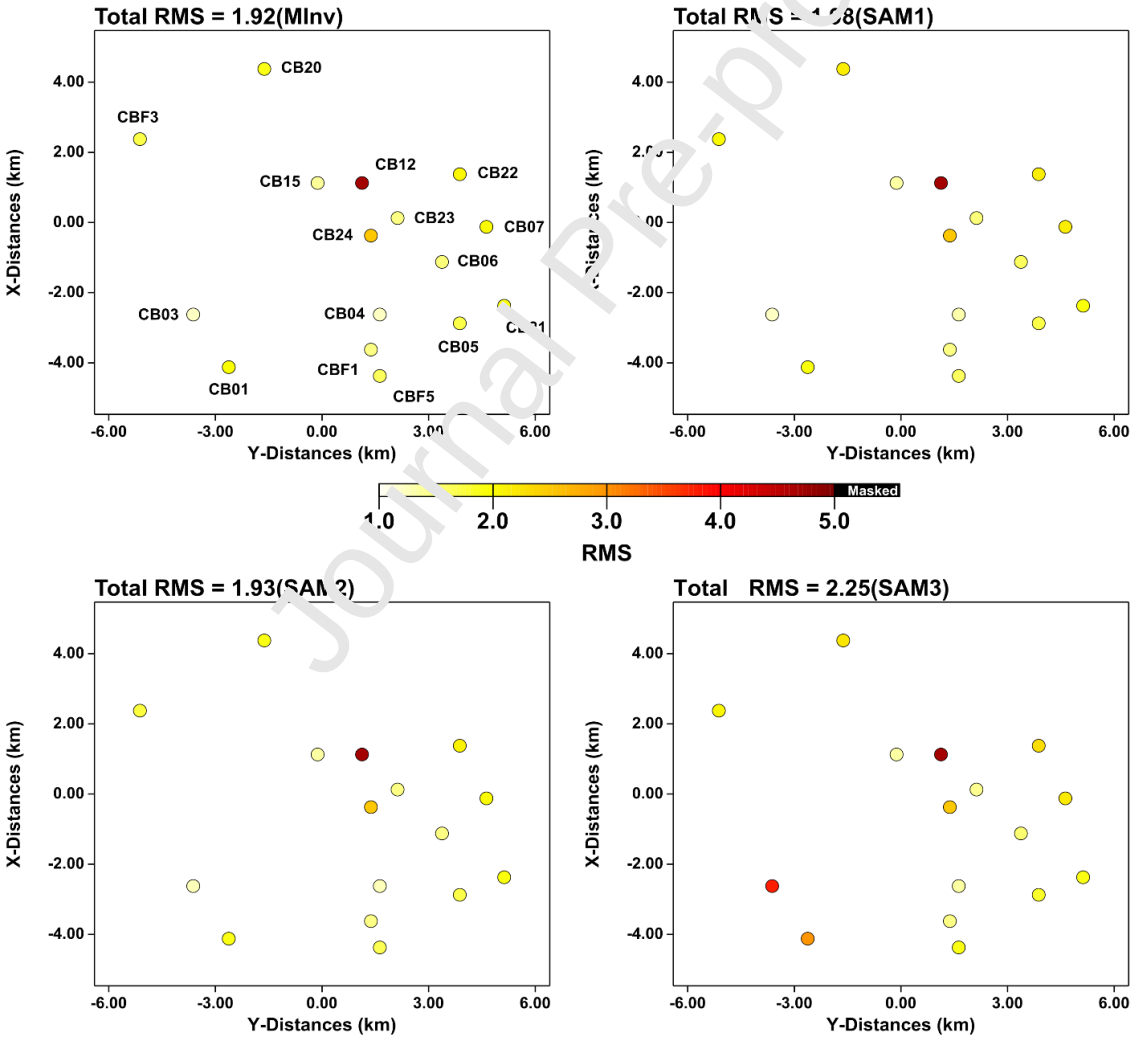

“Magnetotelluric imaging of the Ceboruco Volcano, Nayarit, Mexico.”

By Mario Alberto Fuentes-Arreazola, Diana Núñez, Francisco Javier Núñez-Cornú, Armando Calderón-Moctezuma, Diego Ruiz-Aguilar, José Manuel Romo Jones.

Credit author statement

Mario Alberto Fuentes Arreazola: Conceptualization, Software, Formal analysis, Writing-Original draft preparation.

Diana Núñez: Data Curation, Writing-Review, and Editing.

Francisco Javier Núñez Cornú: Conceptualization, Supervision, Project administration.

Armando Calderón Moctezuma: Software, Formal analysis, Writing-Review, and Editing.

Diego Ruiz-Aguilar: Software, Formal Analysis, Writing-Review, and Editing.

José Manuel Romo Jones: Formal analysis, Writing-Review, and Editing, Project administration.

No conflict of interest statement

The authors declare no conflict of interest.

Declaration of competing for interest

The authors declare that they have no competing financial interests or personal relationships that could have appeared to influence the work reported in this paper.

Tables

Table (1). Sampling frequency recorded at each MT-Station.

Sampling rate [Hz]	ID-Magnetotelluric Station
32768	CB01, CB03, CB04, CB05, CB06, CB07, CB12, CB15, CB20, CB21, CB22, CB23, CB24, CBF1, CBF3, CBF5, CB02*, CB08*, CB11*, CB14*, CB16*, CB17*, CB18*, CBF2*
2048	CB01, CB03, CB04, CB05, CB06, CB07, CB12, CB20, CB21, CB22, CB23, CBF3, CB14*, CB17*, CB18*, CBF2
512	CB01, CB04, CB06, CB07, CB12, CB20, CB21, CB23, CBF3, CBF5
128	CB03, CB05, CB22

Note: MT-Stations denoted with (*) were not considered in this study.